SIAM J. Applied Dynamical Systems
Vol. 14, No. 3, pp. 1518–1557

Understanding and Distinguishing Three-Time-Scale Oscillations: Case Study in a Coupled Morris–Lecar System*

Pingyu Nan†, Yangyang Wang‡, Vivien Kirk†, and Jonathan E. Rubin‡

Abstract. Many physical systems feature interacting components that evolve on disparate time scales. Significant insights about the dynamics of such systems have resulted from grouping time scales into two classes and exploiting the time scale separation between classes through the use of geometric singular perturbation theory. It is natural to expect, however, that some dynamic phenomena cannot be captured by a two-time-scale decomposition. In this work, we are motivated by applications in neural dynamics to focus on a model consisting of a pair of Morris–Lecar systems coupled so that there are three time scales in the full system. We demonstrate that two approaches previously developed in the context of geometric singular perturbation theory for the analysis of two-time-scale systems extend naturally to the three-time-scale setting, where they complement each other nicely. Our analysis explains the dynamic mechanisms underlying solution features in the three-time-scale model. By comparison with certain two-time-scale versions of the same system, we identify some solution properties that truly require three time scales and thus can be viewed as indicators that the presence of three time scales in a system is functionally relevant.

Key words. fast-slow systems, multiple time scales, oscillations, geometric singular perturbation theory

AMS subject classifications. 34C15, 34C26, 34E15, 37N25, 92B25

DOI. 10.1137/140985494

1. Introduction.

Many physical quantities have characteristic rates at which they tend to evolve. For example, people do not gain meters in height overnight, but rather grow over weeks, months, and years. Identifying relevant time scales is a useful step in modeling physical systems using any sort of dynamic framework. In mathematical analysis in particular, the time scales in a system of differential equations are often grouped into a small number of classes, so that limits can be taken and the assumptions of certain mathematical techniques can be satisfied; the aim is to use knowledge of the limit system(s) to gain information about the behavior of the original system. Examples of this approach are ubiquitous in the literature, with ideas applicable to systems in which time scales can be grouped into two classes being particularly well developed. However, there have been fewer reported studies that analyze dynamics involving evolution on three distinct time scales. Even fewer works have examined decisions about how to group time scales (for example, whether to use two or three classes), a decision that can arise both in the mathematical treatment of models and in the development

*Received by the editors September 8, 2014; accepted for publication (in revised form) by B. Sandstede June 25, 2015; published electronically September 1, 2015. This work was partially supported by U.S. NSF awards DMS 1021701 and DMS 1312508 and by the Marsden Fund of the Royal Society of NZ.
http://www.siam.org/journals/siads/14-3/98549.html
†Department of Mathematics, University of Auckland, Private Bag 92019, Auckland, New Zealand (pnan011@aucklanduni.ac.nz, v.kirk@auckland.ac.nz).
‡Department of Mathematics, University of Pittsburgh, 301 Thackeray Hall, Pittsburgh, PA 15260 (yaw23@pitt.edu, jonrubin@pitt.edu).

of mathematical models based on experimental observations. Our goal in this paper is to do both of these things, with a focus on a certain minimal model.

This work was originally motivated by efforts to understand oscillatory dynamics in neurons. It is well established that neural processes can evolve over very different time scales. For instance, the membrane potential of a neuron typically oscillates with a period on the order of milliseconds in response to opening and closing of ion channels in the membrane [6]. The ion channels, in turn, may have conductances that are modulated by much slower variations in the concentration of cytoplasmic calcium (Ca^{2+}) ions. Typical simple models of membrane potential oscillations (ignoring conductance modulation by Ca^{2+}) have at least two time scales [12], as do typical simple models of oscillations in intracellular Ca^{2+} [16], and thus models that combine these two processes typically involve three or more time scales. These combined models can have highly complicated solutions [21], and one challenge is to determine the mathematical mechanisms underlying the dynamics. We are particularly interested in knowing how much of the complication results from the presence of three or more time scales in the model and how much is, rather, a reflection of the models being relatively high-dimensional nonlinear systems with many parameters.

As a first step in addressing such issues, we adopt the approach of constructing and analyzing a minimal model that has three time scales explicitly built into it. This approach shares some similarities with that taken in [2, 30, 18], but we focus on some different aspects of solutions and their time scale dependence; a detailed discussion of the similarities and differences is in section 5. We start with two copies of the Morris–Lecar (ML) equations [20, 23] and couple them in a simple way. The ML equations are a two-dimensional system of ordinary differential equations often used as a simple qualitative model of membrane potential oscillations; one of the variables of the model represents the membrane potential, and the other represents inactivation of a family of ion channels in the membrane. With typical parameter values, the model has two time scales, with the membrane potential evolving much faster than the state of the ion channels. We choose to couple two copies of the two-dimensional model, not because we believe that the system so obtained is a physiologically accurate model of neuronal dynamics, but because it gives us a model where we can easily control the time scales; since the dynamics of a single ML oscillator is relatively well understood [23, 29], we can use the coupled system to investigate which features of the dynamics arise directly from the time scale structure of the model.

Our coupled ML system takes the form

$$C_1\frac{dV_1}{dt} = I_1 - g_{\mathrm{Ca}}m_\infty(V_1)(V_1 - V_{\mathrm{Ca}}) - g_{\mathrm{K}}w_1(V_1 - V_{\mathrm{K}}) - g_{\mathrm{L}}(V_1 - V_{\mathrm{L}}) - g_{\mathrm{syn}}S(V_2)(V_1 - V_{\mathrm{syn}}), \tag{1.1a}$$

$$\frac{dw_1}{dt} = \phi_1(w_\infty(V_1) - w_1)/\tau_w(V_1), \tag{1.1b}$$

$$C_2\frac{dV_2}{dt} = I_2 - g_{\mathrm{Ca}}m_\infty(V_2)(V_2 - V_{\mathrm{Ca}}) - g_{\mathrm{K}}w_2(V_2 - V_{\mathrm{K}}) - g_{\mathrm{L}}(V_2 - V_{\mathrm{L}}), \tag{1.1c}$$

$$\frac{dw_2}{dt} = \phi_2(w_\infty(V_2) - w_2)/\tau_w(V_2)\,, \tag{1.1d}$$

Table 1

The values of the parameters in the model given by (1.1) and (1.2).

Parameter values					
C_1	8 μF/cm^2	I_1	0 μA/cm^2	ϕ_1	0.01
C_2	100 μF/cm^2	I_2	60 μA/cm^2	ϕ_2	0.001
V_{Ca}	120 mV	g_{Ca}	4 mS/cm^2	K_1	-1.2 mV
V_{K}	-84 mV	g_{K}	8 mS/cm^2	K_2	18 mV
V_{L}	-60 mV	g_{L}	2 mS/cm^2	K_3	12 mV
V_{syn}	30 mV	θ_s	-20 mV	K_4	17.4 mV
β	0.5 ms^{-1}	σ_s	10 mV		

with

$$S(V_i) = \alpha(V_i)/(\alpha(V_i) + \beta), \tag{1.2a}$$

$$\alpha(V_i) = 1/(1 + \exp(-(V_i - \theta_s)/\sigma_s)), \tag{1.2b}$$

$$m_\infty(V_i) = 0.5(1 + \tanh((V_i - K_1)/K_2)), \tag{1.2c}$$

$$w_\infty(V_i) = 0.5(1 + \tanh((V_i - K_3)/K_4)), \tag{1.2d}$$

$$\tau_w(V_i) = 1/\cosh((V_i - K_3)/2K_4)\,, \tag{1.2e}$$

where $i = 1, 2$. The parameter g_{syn} controls the coupling between the two oscillators, which we choose for simplicity to be unidirectional such that the dynamics of (V_2, w_2) affects the dynamics of (V_1, w_1) but not vice versa; we refer to $S(V_2)$ as the coupling function. Several values of g_{syn}, with units of mS/cm^2, will be considered, while other parameters will be fixed at the values shown in Table 1, selected so that there is clear separation of time scales between V_i (fast) and w_i (slow) in each oscillator and so that w_1 and V_2 evolve at comparable rates. In a more biologically realistic model for calcium and voltage interactions, V_1 might represent membrane potential and V_2 intracellular calcium concentration, and the physical units of some parameters in Table 1 and details of some terms in the model would need to be altered correspondingly. We work with (1.1)–(1.2) and the units in Table 1 nonetheless, since they provide the appropriate minimal mathematical structure (cf. [2, 30]), and these are the traditional units for the ML system.

In the absence of coupling, each ML oscillator can be tuned to be excitable, with an attracting critical point at relatively low V, or oscillatory, with an attracting limit cycle solution. A transition between these states can be induced by increasing the parameter I_i in the V_i-equation and typically occurs through a saddle node on an invariant circle (SNIC) or an Andronov–Hopf (AH) bifurcation, called a Type I or Type II transition [23], respectively. The specific parameters in Table 1 would yield a Type I transition if I_1 or I_2 were varied, but we keep I_1 and I_2 fixed at values such that when $g_{syn} = 0$, the (V_1, w_1) system is excitable and the (V_2, w_2) system is oscillatory (Figure 1). In this regime, (1.1)–(1.2) has the structure of an intrinsic oscillator, such as intracellular calcium oscillations, driving a conditional oscillator, such as calcium-dependent neuronal membrane potential oscillations. A similar structure was considered in the context of neurosecretory dynamics in [18]. In that work, a slower relaxation oscillation also provided input to a faster conditional oscillator, switching it between excitable and oscillatory states. Importantly, however, the coupling term in that work appeared in the

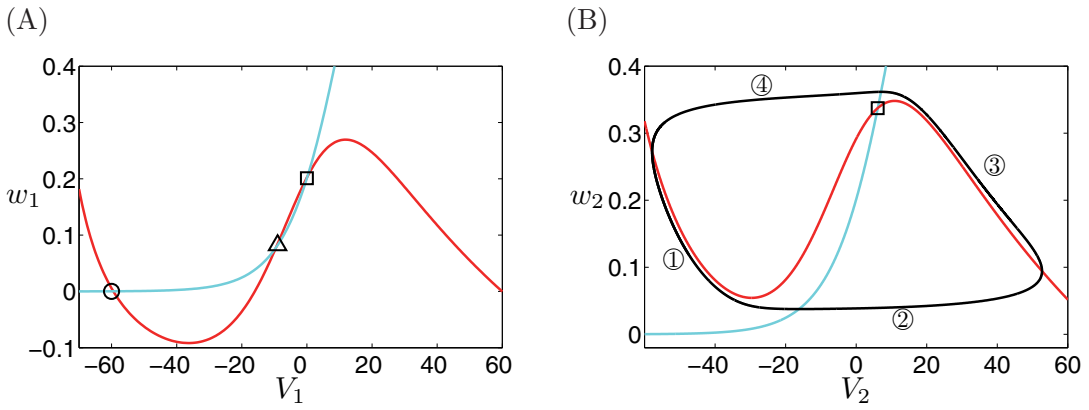

Figure 1. *Baseline phase planes for the two ML systems without coupling. In each plot, the red curve is the V-nullcline and the cyan is the w-nullcline. The hollow circles, triangles, and squares denote equilibrium solutions of sink, saddle, and source type, respectively. The (V_1, w_1) system in* (A) *lacks a periodic solution, while the attracting periodic orbit for the (V_2, w_2) system in* (B) *is shown in black (with counterclockwise flow passing through the numbered regions in increasing order).*

equation for the slow recovery variable (analogous to w_1 in our notation), a difference that results in some qualitatively different dynamical effects, as we will discuss further in section 5.

In this paper, we first explain the mechanisms underlying the dynamics of our model system. In doing so, we consider two viewpoints within the realm of geometric singular perturbation theory (GSPT). In one, we establish the roles of critical and superslow manifolds, within the four-dimensional model phase space, in shaping model dynamics, making heavy use of projections to three dimensions. In the other viewpoint, we link various two-dimensional projections, corresponding either to the phase plane of one ML system or to the slow subsystem of the model, as has often been useful in past studies of the dynamics of synaptically coupled neurons (e.g., [26, 28, 1, 25]). Notation and other preliminaries relating to these approaches are presented in section 2 and the appendix. The system that we study progresses through a variety of oscillatory solutions as the coupling strength g_{syn} is increased. We focus on certain key aspects appearing in the dynamics for three particular values of g_{syn}—the onset of oscillations in the conditional oscillator, the emergence of sustained oscillations, the modulation of oscillation amplitude, and the convergence to an elevated plateau—such that patterns arising for other g_{syn} can be readily understood in terms of these components. The mechanisms underlying these phenomena are analyzed using our two approaches in section 3. Next, in section 4, we revisit the solution types and elucidate which characteristics truly represent three-time-scale features. This analysis involves consideration of certain reductions to two time scales as well as additional analysis of the parameter dependence of solution features in the three-time-scale framework. Our results in this area may be useful for characterizing, developing models of, and analyzing models of experimental data. Finally, section 5 contains a discussion of our results.

2. Preliminaries.

Based on simulations of (1.1)–(1.2) over a range of g_{syn} values, we have selected three fundamental solution types on which to focus our analysis, specifically those obtained by setting g_{syn} to 1.0, 4.1, and 5.1. Time series for the attracting solutions at these

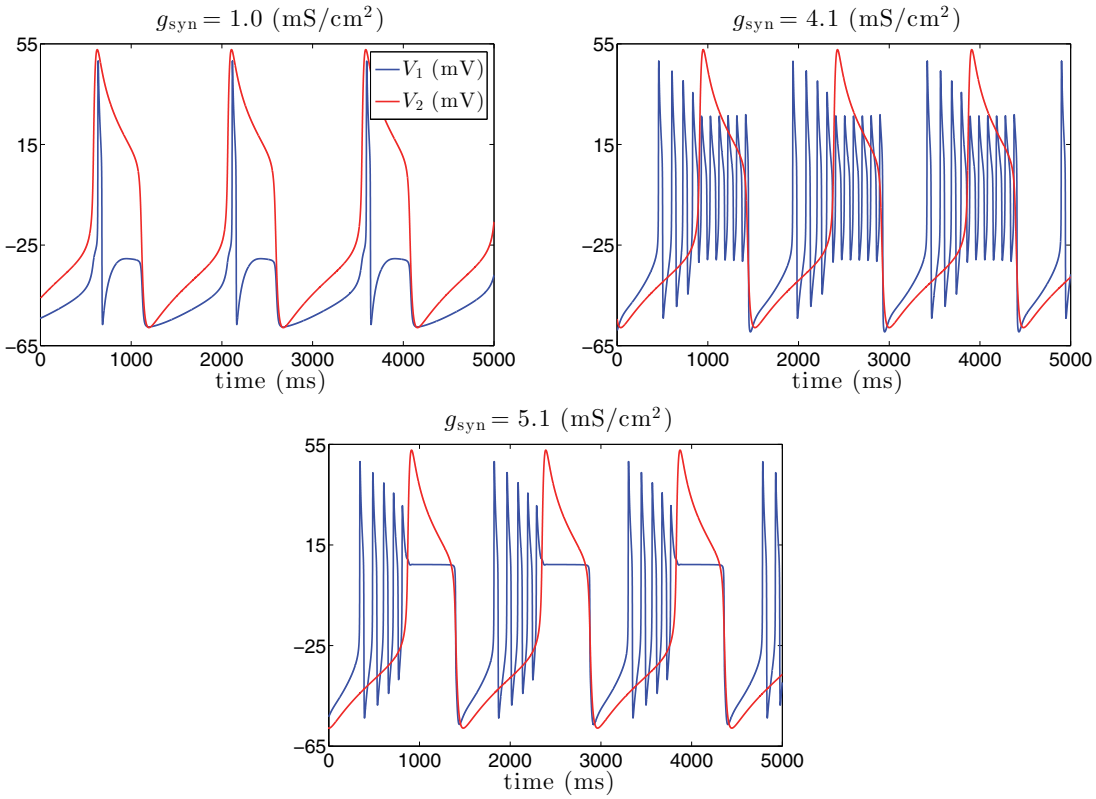

Figure 2. *Time series for attracting solutions of* (1.1)–(1.2) *with parameter values as in Table* 1 *and with the indicated values of* g_{syn}.

values of g_{syn} are shown in Figure 2. We shall see that the properties of these solutions are indicative of the presence of at least three time scales.

Our methods for analysis of the model will depend heavily on exploiting the presence of different time scales. As a first step in the analysis, therefore, it is helpful to rescale the variables so that the important time scales can be explicitly identified. To this end, we define new dimensionless variables (v_1, v_2, τ), and voltage and time scales Q_v and Q_t, respectively, such that

$$V_1 = Q_v \cdot v_1\,, \qquad V_2 = Q_v \cdot v_2\,, \qquad t = Q_t \cdot \tau. \tag{2.1}$$

Note that w_1 and w_2 are already dimensionless in (1.1a)–(1.1d).

Details of the nondimensionalization procedure, including determination of appropriate values for Q_v and Q_t, are given in the appendix. From this process, we obtain a dimensionless system of the form

$$\varepsilon_1 \frac{dv_1}{d\tau} = f_1(v_1, v_2, w_1), \tag{2.2a}$$

$$\frac{dw_1}{d\tau} = g_1(v_1, w_1), \tag{2.2b}$$

$$\frac{dv_2}{d\tau} = f_2(v_2, w_2), \tag{2.2c}$$

$$\frac{dw_2}{d\tau} = \varepsilon_2 g_2(v_2, w_2)\,, \tag{2.2d}$$

with small parameters $\varepsilon_1, \varepsilon_2 \ll 1$, where the functions f_1, f_2, g_1, and g_2 are specified in (6.3) in the appendix. The values of ε_1 and ε_2 can be varied by changing C_1 and ϕ_2, respectively, as shown in (6.2a); the parameter values given in Table 1 yield $\varepsilon_1 = 0.1, \varepsilon_2 = 0.053$.

2.1. Singular limits: Scalings and subsystems. Standard ideas from GSPT [7, 14, 15] are useful in our analysis, although they need to be adapted to allow for the presence of three time scales in our model. Rewriting the time variable τ as t_s, we see that (2.2) has the form

$$\varepsilon_1 \frac{dv_1}{dt_s} = f_1(v_1, v_2, w_1), \tag{2.3a}$$

$$\frac{dw_1}{dt_s} = g_1(v_1, w_1), \tag{2.3b}$$

$$\frac{dv_2}{dt_s} = f_2(v_2, w_2), \tag{2.3c}$$

$$\frac{dw_2}{dt_s} = \varepsilon_2 g_2(v_2, w_2)\,, \tag{2.3d}$$

where f_1, g_1, f_2, g_2 are $O(1)$ functions and ε_1, ε_2 are small parameters. We refer to changes with respect to t_s as evolution on the *slow time scale*. Introducing a superslow time $t_{ss} = \varepsilon_2 t_s$, which changes slowly relative to t_s, we can derive the rescaled system

$$\varepsilon_1\varepsilon_2 \frac{dv_1}{dt_{ss}} = f_1(v_1, v_2, w_1), \tag{2.4a}$$

$$\varepsilon_2 \frac{dw_1}{dt_{ss}} = g_1(v_1, w_1), \tag{2.4b}$$

$$\varepsilon_2 \frac{dv_2}{dt_{ss}} = f_2(v_2, w_2), \tag{2.4c}$$

$$\frac{dw_2}{dt_{ss}} = g_2(v_2, w_2), \tag{2.4d}$$

which evolves on the *superslow time scale*. Alternatively, defining a fast time $t_f = t_s/\varepsilon_1$, which changes quickly relative to t_s, we obtain the rescaled system

$$\frac{dv_1}{dt_f} = f_1(v_1, v_2, w_1), \tag{2.5a}$$

$$\frac{dw_1}{dt_f} = \varepsilon_1 g_1(v_1, w_1), \tag{2.5b}$$

$$\frac{dv_2}{dt_f} = \varepsilon_1 f_2(v_2, w_2), \tag{2.5c}$$

$$\frac{dw_2}{dt_f} = \varepsilon_1\varepsilon_2 g_2(v_2, w_2), \tag{2.5d}$$

which evolves on the *fast time scale*.

There are several possible singular limits that can be taken in (2.3)–(2.5), yielding an array of subsystems. We will use the term *reduced problem* to refer to a subsystem that is exposed by a limit that eliminates dynamics faster than the baseline time scale. The phrase *layer problem* will refer to a system obtained by eliminating dynamics slower than the baseline. Since a reduced problem may have more than one time scale, we can define a layer problem for a reduced problem, and we will refer to the resulting system as a *reduced layer problem*. These terms will become clearer as we apply them to specific systems below.

Fixing $\varepsilon_2 > 0$ and taking $\varepsilon_1 \to 0$ in (2.5) yields a system that describes the dynamics of the fast variable, v_1, for fixed values of the other variables,

$$\frac{dv_1}{dt_f} = f_1(v_1, w_1, v_2). \tag{2.6}$$

We call this limit the *fast layer problem*, and refer to the corresponding dynamics as the *fast flow*. We define the critical manifold $\mathcal{M}_s$ to be the manifold of equilibrium points of the fast layer problem, i.e.,

$$\mathcal{M}_s := \{(v_1, v_2, w_1, w_2) : f_1(v_1, v_2, w_1) = 0\}. \tag{2.7}$$

Although $\mathcal{M}_s$ is a three-dimensional manifold in (v_1, w_1, v_2, w_2) space, it does not depend on w_2. We can solve $f_1(v_1, v_2, w_1) = 0$ for w_1 as a function of v_1 and v_2 and can therefore represent $\mathcal{M}_s$ as

$$w_1 = F_1(v_1, v_2) \tag{2.8}$$

for a function F_1. This relation allows us to readily visualize the projection of $\mathcal{M}_s$ onto (v_1, v_2, w_1)-space. It is well known [7] that, for sufficiently small $\varepsilon_1 > 0$, normally hyperbolic parts of $\mathcal{M}_s$ each perturb to a locally invariant manifold called a *slow manifold*, on which w_1 is given by an $O(\varepsilon_1)$-perturbation of F_1; we simply use $\mathcal{M}_s$ as a convenient numerical approximation of these slow manifolds.

Taking the same limit, i.e., $\varepsilon_1 \to 0$ with $\varepsilon_2 > 0$, in (2.3) yields a system that describes the dynamics of w_1, v_2, w_2 restricted to the surface $\mathcal{M}_s$,

$$\frac{dw_1}{dt_s} = g_1(v_1, w_1), \tag{2.9a}$$

$$\frac{dv_2}{dt_s} = f_2(v_2, w_2), \tag{2.9b}$$

$$\frac{dw_2}{dt_s} = \varepsilon_2 g_2(v_2, w_2), \tag{2.9c}$$

subject to the constraint $f_1(v_1, v_2, w_1) = 0$. Since it is obtained by eliminating the fast flow, we call this system the *slow reduced problem*. It is itself a multiple-time-scale problem, since the slow and superslow time scales are still both present. It is convenient to further separate scales by letting $\varepsilon_2 \to 0$ in (2.9); doing so yields the *slow reduced layer problem*,

$$\frac{dw_1}{dt_s} = g_1(v_1, w_1), \tag{2.10a}$$

$$\frac{dv_2}{dt_s} = f_2(v_2, w_2), \tag{2.10b}$$

which describes the dynamics of the slow variables w_1 and v_2 for fixed values of w_2, with all variables restricted to $\mathcal{M}_s$. Since it takes place entirely on the slow time scale, we refer to the corresponding dynamics as the *slow flow*.

Alternatively, fixing $\varepsilon_1 > 0$ and taking $\varepsilon_2 \to 0$ in (2.3) or (2.5) yields the *slow layer problem*, which is a different layer problem from (2.10). Starting from (2.3) yields the slow layer problem in the form

$$\varepsilon_1 \frac{dv_1}{dt_s} = f_1(v_1, v_2, w_1)\,, \tag{2.11a}$$

$$\frac{dw_1}{dt_s} = g_1(v_1, w_1)\,, \tag{2.11b}$$

$$\frac{dv_2}{dt_s} = f_2(v_2, w_2)\,. \tag{2.11c}$$

System (2.11) still includes two distinct time scales, and we can manipulate the system to obtain either the fast layer problem (2.6), by rescaling time and taking a limit, or the slow reduced layer problem (2.10), by taking a limit. We define the *superslow manifold*, $\mathcal{M}_{ss}$, to be the set of equilibrium points of the slow layer problem, i.e.,

$$\mathcal{M}_{ss} := \{(v_1, v_2, w_1, w_2) : f_1(v_1, v_2, w_1) = g_1(v_1, w_1) = f_2(v_2, w_2) = 0\}\,. \tag{2.12}$$

Note that $\mathcal{M}_{ss}$ is a subset of $\mathcal{M}_s$. Similarly to $\mathcal{M}_s$, the normally hyperbolic parts of $\mathcal{M}_{ss}$ perturb to nearby locally invariant manifolds for ε_2 sufficiently small, and we approximate the collection of these manifolds by $\mathcal{M}_{ss}$.

Taking the same limit in (2.4), i.e., $\varepsilon_2 \to 0$ with $\varepsilon_1 > 0$, gives a system that describes the dynamics of w_2 restricted to $\mathcal{M}_{ss}$,

$$\frac{dw_2}{dt_{ss}} = g_2(v_2, w_2)\,. \tag{2.13}$$

We call this system the *superslow reduced problem* and refer to the corresponding dynamics as the *superslow flow*.

There is one more limiting system that turns out to be important for the dynamics we consider. We define the three-dimensional manifold, $\mathcal{M}_\sigma$, by

$$\mathcal{M}_\sigma := \{(v_1, w_1, v_2, w_2) : f_2(v_2, w_2) = 0\}.$$

Because the dynamics of (v_2, w_2) decouples from (v_1, w_1) in (2.2), we can find a function F_2 such that

$$w_2 = F_2(v_2) \tag{2.14}$$

on $\mathcal{M}_\sigma$. Differentiation of (2.14) with respect to t_s yields

$$\frac{dw_2}{dt_s} = F_2'(v_2)\frac{dv_2}{dt_s}.$$

This equation can be combined with (2.3) to obtain the three-time-scale system

$$\varepsilon_1 \frac{dv_1}{dt_s} = f_1(v_1, w_1, v_2)\,, \tag{2.15a}$$

$$\frac{dw_1}{dt_s} = g_1(v_1, w_1)\,, \tag{2.15b}$$

$$\frac{dv_2}{dt_s} = \frac{\varepsilon_2 g_2(v_2, F_2(v_2))}{F_2'(v_2)} \tag{2.15c}$$

describing the dynamics on $\mathcal{M}_\sigma$, away from its folds (to leading order in ε_2; see Remark 2.1). An analogous system was used heavily in the analysis of three-time-scale dynamics in [18].

Remark 2.1. *Just as $\mathcal{M}_s$ is defined in the singular limit and perturbs to a nearby locally invariant manifold for $0 < \varepsilon_1 \ll 1$, $\mathcal{M}_\sigma$ perturbs to a nearby locally invariant manifold for $0 < \varepsilon_2 \ll 1$. This manifold is given by $w_2 = F_2(v_2) + O(\varepsilon_2)$, and additional terms should appear in the v_2 equation in (2.15) to reflect this perturbation, but these are higher order in ε_2 and we omit them.*

It will be useful to work with two systems defined from (2.15). First, taking $\varepsilon_1 \to 0$ yields the slow reduced problem for (2.15) governing the dynamics on $\mathcal{M}_s \cap \mathcal{M}_\sigma$. Taking the subsequent limit $\varepsilon_2 \to 0$ gives the slow reduced layer problem for (2.15), namely,

$$\frac{dw_1}{dt_s} = g_1(v_1, w_1)\,, \tag{2.16}$$

on $\mathcal{M}_s \cap \mathcal{M}_\sigma$; note that this equation is consistent with (2.10) with $f_2 = 0$, although it cannot be obtained by taking a limit in (2.10) directly.

Second, taking $\varepsilon_2 \to 0$ directly in (2.15) gives

$$\varepsilon_1 \frac{dv_1}{dt_s} = f_1(v_1, w_1, v_2)\,, \tag{2.17a}$$

$$\frac{dw_1}{dt_s} = g_1(v_1, w_1)\,. \tag{2.17b}$$

System (2.17) is the slow layer problem for (2.15). To distinguish it from (2.11), we will also call (2.17) the *v_2-frozen system*, with solutions that we call *v_2-frozen solutions*. Similarly, when it is helpful, we will refer to (2.16) as the *v_2-frozen system reduced problem* and (2.6) as the *v_2-frozen system layer problem*, since these can be obtained through appropriate limits from (2.17).

For reference, we summarize the subsystems that are useful for describing the dynamics of (2.2) in Table 2.

Within the context of GSPT, the usual way to proceed from here is to construct *singular periodic orbits* by concatenating solution segments of singular limit systems. For instance, within a two-time-scale setting and for a system with a cubic-shaped critical manifold, one might be able to construct a singular closed orbit by concatenating in order a solution of the (fast) layer problem, a solution of the (slow) reduced problem, a second solution of the layer problem, and a second solution of the reduced problem, as illustrated in Figure 3. Then, depending on the details of the dynamics and the structure of the critical manifold where

Table 2
Subsystems for (2.2).

Equation	System name	Dynamic variables	Baseline time scale	Domain
(2.6)	fast layer / v_2-frozen layer	v_1	t_f	$\mathbb{R}^4$
(2.9)	slow reduced	w_1, v_2, w_2	t_s	$\mathcal{M}_s$
(2.10)	slow reduced layer	w_1, v_2	t_s	$\mathcal{M}_s$
(2.17)	slow layer on $\mathcal{M}_\sigma$ / v_2-frozen	v_1, w_1	t_s	$\mathcal{M}_\sigma$
(2.16)	slow reduced layer on $\mathcal{M}_\sigma$ / v_2-frozen reduced	w_1	t_s	$\mathcal{M}_s \cap \mathcal{M}_\sigma$
(2.13)	superslow reduced	w_2	t_{ss}	$\mathcal{M}_{ss} \subset \mathcal{M}_s$

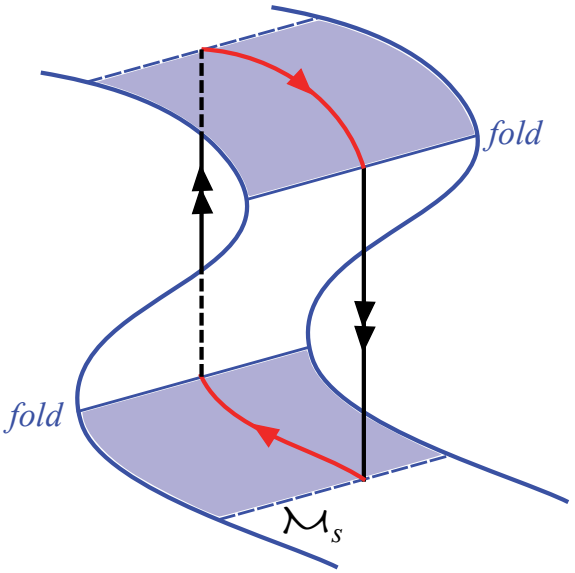

Figure 3. *Schematic diagram showing construction of a singular periodic orbit by concatenation of solution segments for singular limit systems. The cubic-shaped surface is the critical manifold, $\mathcal{M}_s$. Solution segments shown in black, corresponding to the fast layer problem, jump between sheets of the critical manifold. Solution segments shown in red, coming from the slow reduced problem, lie on the critical manifold.*

the connections between the slow and fast segments occur, such a singular oscillation will generically perturb, as we move away from the singular limit, to a periodic solution of the full problem. In this manner, one is able to use the singular limit systems to understand the nature of oscillations in the full system. Further details of the method appear elsewhere (e.g., [14, 5]).

A similar method could also be used to explain the oscillations seen in three-time-scale systems, although the process would be more complicated since there are more than two singular limit systems to be considered. In this paper, for reasons of brevity, we choose not to show detailed constructions of singular orbits and subsequent analysis of how these perturb. Instead, we appeal to intuition based on the way the technique works in two-time-scale systems to explain the mechanisms underlying solutions generated in simulations done with a separation of scales but away from a true singular limit. In the following discussion, we will show orbits of the full system and refer to different segments of them as being governed

by the subsystems in Table 2 and evolving under the fast, slow, or superslow flow; by this we mean that, in an appropriate singular limit, these segments will converge to nearby solutions of these subsystems.

Remark 2.2. *We could have chosen alternative values of* C_1, C_2, ϕ_1, ϕ_2 *to impose a wider separation of time scales. We opted to use the values specified in Table 1, corresponding to* $\varepsilon_1 = 0.1$ *and* $\varepsilon_2 = 0.053$*, to show that extreme time scale separation is not necessary in order for the issues that we consider to arise. This point will come up again later in the paper, when proximity of time scales renders certain analysis steps more subtle.*

In the two-time-scale context, a crucial step in determining the nature of the solution that arises from a perturbation of a singular periodic orbit is to establish the type of points that occur at the transitions from slow to fast segments of the singular orbit when these occur on fold curves. Two types of point are commonly seen: *jump points* and *folded singularities* [5]. Singular orbits containing only jump points perturb in a straightforward way to orbits that transition smoothly from slow to fast motion near the jump points, such as relaxation oscillations. However, singular orbits containing folded singularities may perturb to more complicated oscillations, including orbits with subthreshold oscillations such as mixed-mode oscillations [5].

Similar considerations are also relevant for three-time-scale systems, although once again the situation is complicated by the existence of more than two singular limit systems. Since $\mathcal{M}_s$ is a three-dimensional surface, fold points of $\mathcal{M}_s$ lie on two-dimensional surfaces within $\mathcal{M}_s$ defined by

$$L_s := \left\{ (v_1, v_2, w_1, w_2) \in \mathcal{M}_s : \ \frac{\partial f_1}{\partial v_1}(v_1, w_1, v_2) = 0 \right\} \tag{2.18}$$

or, equivalently, as

$$L_s := \left\{ (v_1, v_2, w_1, w_2) : \ w_1 = F_1(v_1, v_2), \ \frac{\partial F_1}{\partial v_1} = 0 \right\}, \tag{2.19}$$

where F_1 was defined in (2.8).

Folded singularities for three-time-scale systems have not been comprehensively studied, although [18] classifies the folded singularities in a particular three-dimensional, three-time-scale system by extending ideas from two-time-scale systems, and [32] extends the concepts developed for two-time-scale systems with two slow variables to systems with three or more slow variables; ideas related to both of these approaches appear in [31], where a degenerate type of folded singularity that arises naturally in three-time-scale systems is identified and some analysis of the related dynamics is given.

In the usual manner, we define the desingularized slow reduced problem by differentiating the algebraic equation defining $\mathcal{M}_s$ (i.e., $f_1(v_1, v_2, w_1) = 0$) and rescaling time using $\tau_s = (\partial F_1/\partial v_1) t_s$, yielding

$$\frac{dv_1}{d\tau_s} = g_1(v_1, w_1) - \frac{\partial F_1}{\partial v_2} f_2(v_2, w_2), \tag{2.20a}$$

$$\frac{dv_2}{d\tau_s} = \frac{\partial F_1}{\partial v_1} f_2(v_2, w_2), \tag{2.20b}$$

$$\frac{dw_2}{d\tau_s} = \varepsilon_2 \frac{\partial F_1}{\partial v_1} g_2(v_2, w_2)\,. \tag{2.20c}$$

We then look for equilibria of (2.20) that are not equilibria of the full system; these are what we refer to as folded singularities of $\mathcal{M}_s$. We find that they lie on one-dimensional curves within L_s defined by

$$FS := \left\{ (v_1,\, v_2,\, w_1,\, w_2) \in L_s :\, g_1(v_1, w_1) - \frac{\partial F_1}{\partial v_2}(v_1, v_2) f_2(v_2, w_2) = 0 \right\}. \tag{2.21}$$

Away from $\mathcal{M}_{ss}$, the linearization of (2.20) at a folded singularity has one zero eigenvalue (due to there being a curve of folded singularities, as in [32]) and two other eigenvalues; the folded singularities can be classified using these other eigenvalues, as in [18, 32]. As we will see, the location and type of folded singularities within $\mathcal{M}_s$ depend on g_{syn}. We note that points where $\mathcal{M}_{ss}$ and L_s intersect are always folded singularities since $g_1 = f_2 = 0$ on $\mathcal{M}_{ss}$; some discussion of this degenerate type of folded singularity is contained in [31].

Since $\mathcal{M}_{ss}$ is a one-dimensional subset of $\mathcal{M}_s$, fold points of $\mathcal{M}_{ss}$ occur at isolated points; these are located on the set

$$L_{ss} := \left\{ (v_1,\, v_2,\, w_1,\, w_2) \in \mathcal{M}_{ss} :\, \frac{\partial f_2}{\partial v_2}(v_2, w_2) = 0 \text{ or } \frac{\partial f_1}{\partial v_1}\frac{\partial g_1}{\partial w_1} - \frac{\partial f_1}{\partial w_1}\frac{\partial g_1}{\partial v_1} = 0 \right\}. \tag{2.22}$$

For all values of g_{syn} that we consider below, points that satisfy the latter condition lie on the middle sheet of $\mathcal{M}_s$ and hence will not play a role in the dynamics, and points that satisfy the former condition are jump points.

2.2. Effect of coupling. When $g_{syn} = 0$, our model decouples into two systems, each of which has two variables and a two-time-scale structure. For the parameter values we have chosen, the nullclines for the uncoupled systems are qualitatively as shown in Figure 1. Each v-nullcline is cubic shaped, with outer branches that are attracting relative to the v dynamics and a repelling inner branch. When solutions are near the outer branch with lower (resp., higher) v values, we say that the system is in the silent (resp., active) phase.

Since the coupling in our system is unidirectional, the oscillations in (v_2, w_2) are independent of the value of g_{syn} and of the dynamics of v_1 and w_1; they are standard relaxation oscillations consisting of a superslow excursion through the silent phase (Figure 1B, ①), a slow jump away from the v_2-nullcline up to the active phase (Figure 1B, ②), a superslow excursion through the active phase (Figure 1B, ③), and a slow jump back to the silent phase (Figure 1B, ④). By contrast, v_1 and w_1 depend on g_{syn} and, if $g_{syn} > 0$, on v_2 and w_2. For positive g_{syn} we find it helpful to consider the phase plane for the v_2-frozen system (2.17) for various fixed values of v_2; this is a reasonable approach to take when v_2 is in a superslow phase, i.e., if the dynamics is close to $\mathcal{M}_\sigma$. Figure 4 shows configurations of the v_1- and w_1-nullclines for (2.17) for several different values of v_2 with $g_{syn} = 5.1$. Note that the v_1-nullcline satisfies (2.8) and is in fact a section of $\mathcal{M}_s$.

Continuing in this spirit, bifurcation diagrams can be obtained for (2.17) using v_2 as the bifurcation parameter. Examples are shown in Figure 5 for several values of g_{syn}. For $g_{syn} = 4.1$ and $g_{syn} = 5.1$, several families of periodic orbits are seen. The first is almost invisible on the scale of Figure 5; as v_2 is increased a branch of unstable small amplitude

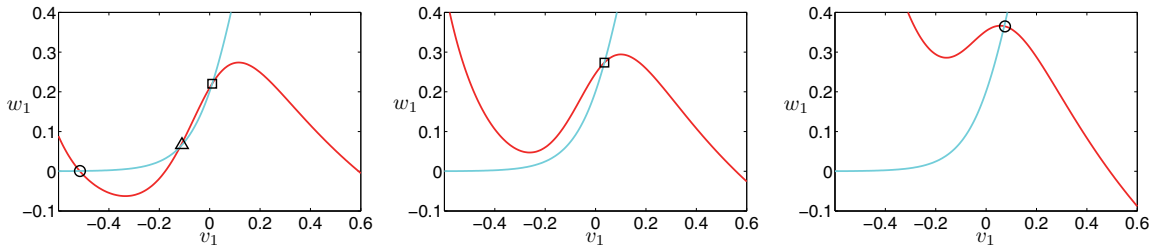

Figure 4. *Nullclines for v_1 (red) and w_1 (cyan) for the v_2-frozen system (2.17). The red curve is a slice through $\mathcal{M}_s$ taken at a fixed v_2 and restricted to the (v_1, w_1) plane. The cyan curve is the restriction of the w_1-nullcline to the (v_1, w_1) plane. Varying v_2 changes the red curve but not the cyan curve. From left to right: $v_2 = -0.7, -0.4, 0.2$, all with $g_{syn} = 5.1$. Circles, triangles, and squares denote equilibria of (2.17) of sink, saddle, and source type, respectively.*

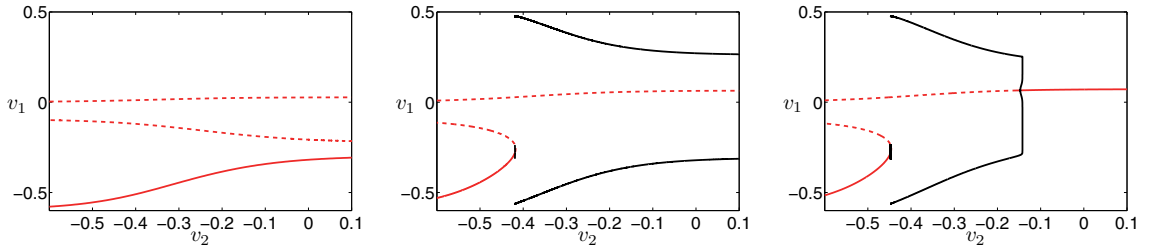

Figure 5. *Bifurcation diagrams for (2.17) with v_2 as a parameter. From left to right, $g_{syn} = 1.0, 4.1, 5.1$. Solid (resp., dashed) red curves indicate stable (resp., unstable) equilibria, and black curves indicate periodic solutions (stability not indicated).*

periodic orbits is created in a homoclinic bifurcation involving the middle branch of equilibria and is destroyed in a subcritical AH bifurcation of the lower branch of equilibria. A second family of stable periodic orbits of much larger amplitude is created in a homoclinic bifurcation also involving the middle branch of equilibria. For $g_{syn} = 5.1$, but not 4.1, this family of orbits terminates for larger v_2 when it coalesces with a third family of unstable periodic solutions born in a subcritical AH bifurcation at relatively large v_2. For $g_{syn} = 4.1$, even with the coupling function $S(v_2)$ set to its upper limit of 1, the upper equilibrium point of (2.17) remains unstable and the stable periodic orbits persist as $v_2 \to \infty$.

Allowing both g_{syn} and v_2 to vary, we find bifurcation curves in the (v_2, g_{syn}) parameter plane, as illustrated in Figure 6. The green (resp., blue) curve in the left panel is the curve of AH bifurcations on the lower (resp., upper) branch of equilibria. These approach horizontal asymptotes as v_2 increases; the lower asymptote is at $g_{syn} \approx 1.0319 =: \tilde{g}$, while the upper asymptote is at $g_{syn} \approx 4.2628 =: \bar{g}$. Existence of the upper asymptote implies that the (v_1, w_1) system will not oscillate for any fixed $g_{syn} > \bar{g}$ if v_2 is fixed at a large enough value; this is illustrated in the right panel of Figure 5. The onset of stable oscillations, on the other hand, is not directly tied to the green AH curve, since that curve relates to the family of unstable oscillations near the lower branch of equilibria. To identify the onset of stable oscillations, we compute the curve of homoclinic bifurcations through which the stable large amplitude oscillations arise as v_2 increases. It turns out that this curve lies extremely close to

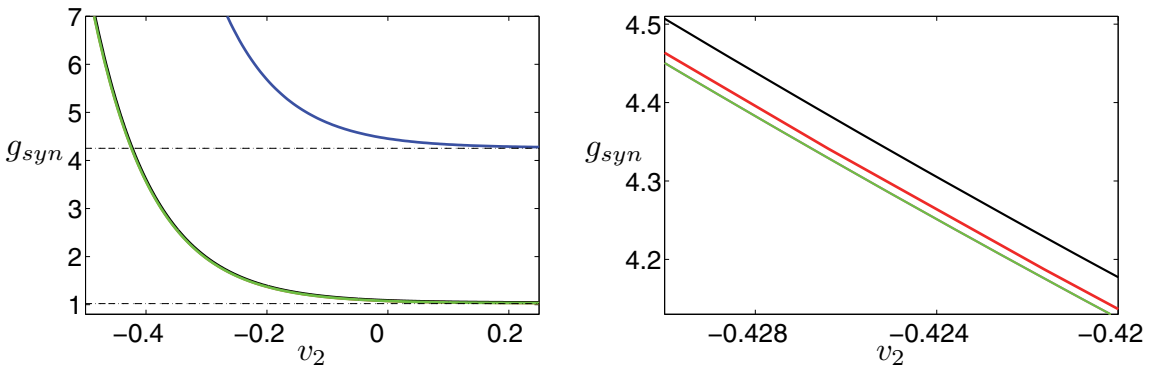

Figure 6. *Bifurcation curves for (2.17) in (v_2, g_{syn}) parameter space. Left: Two curves of AH bifurcations (green, lower v_1; blue, higher v_1) and their horizontal asymptotes (dashed). Right: Enlargement of part of left panel showing, in order of increasing v_2 and g_{syn}, part of the lower AH curve (green), two overlapping homoclinic bifurcation curves (red), and, for comparison, the curve of saddle-node bifurcations that occurs at relatively low v_1 (black).*

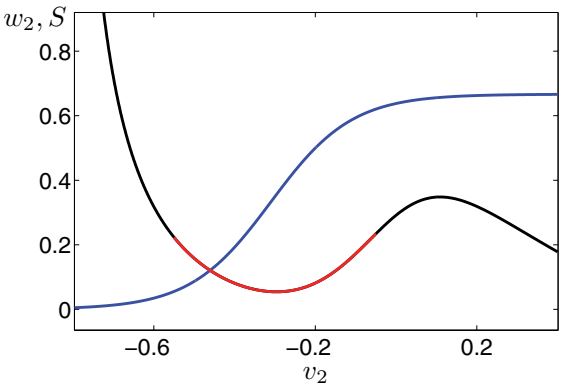

Figure 7. *Graph of $S(v_2)$ (blue) and locus of the v_2-nullcline (black/red). The red section of the v_2-nullcline indicates the range of v_2 values over which $S(v_2)$ is steeply sloped.*

the lower AH curve (compare the red and green curves in the right panel of Figure 6), with approximately the same asymptote. Thus, for $g_{syn} < \tilde{g}$, there is no value at which v_2 can be fixed to yield oscillations in (v_1, w_1), while for $g_{syn} \in (\tilde{g}, \bar{g})$ oscillations occur for all v_2 above the homoclinic bifurcation.

The structure of the bifurcation set in Figure 6 stems in part from the form of the coupling function $S(v_2)$ in (1.1), as defined in (1.2) and shown in Figure 7. For v_2 sufficiently small or sufficiently large, $S(v_2)$ varies little in response to changes in v_2, whereas for intermediate values of v_2, $S(v_2)$ changes rapidly with v_2 (red in Figure 7). As a consequence, changes of v_2 within the intermediate interval result in significant effects on the v_1 equation, while changes in v_2 outside of this domain have little effect. This saturation of S explains why the horizontal asymptotes in Figure 6 exist and why certain bifurcations cannot be achieved by increasing

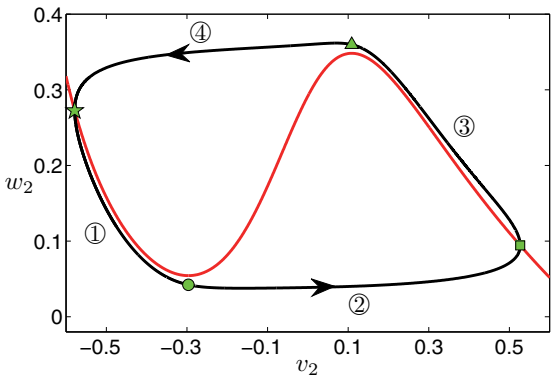

Figure 8. *Attracting dynamics in (v_2, w_2)-space. The green symbols mark the approximate points of transition between the slow and superslow sections of the oscillation: the square and star mark the transitions from slow to superslow motion, and the circle and triangle mark the transitions from superslow to slow motion. The circled numbers label the sections of the oscillation, using the same convention as in Figure* 1B.

v_2 in (2.17) if g_{syn} is not sufficiently large. Figure 7 also shows where the steepest part of S lies relative to the v_2-nullcline. We see that $S(v_2)$ is sensitive to changes in v_2 over the silent phase and over jumps between phases but is insensitive to v_2 in the active phase for the parameter values we use.

As noted above, the (v_2, w_2) dynamics is not dependent on (v_1, w_1) or on g_{syn}; with parameters fixed as in Table 1, the (v_2, w_2) variables trace out a relaxation oscillation, shown in Figure 1B. It will be helpful to define some reference points along the relaxation oscillation. Figure 8 shows the (v_2, w_2) oscillation from Figure 1B plotted in nondimensionalized coordinates, with green symbols marking points at the transition between the four different sections of the oscillation. These symbols have the same interpretation in all the figures and analysis that follow.

3. Analysis of three-time-scale solutions.

Simulation of (2.2) over a range of parameter values yields a variety of solution behaviors, with variation in g_{syn} giving a particularly nice progression of features. We focus our analysis on three values of g_{syn}; these values highlight the distinct combinations of dynamic mechanisms that can arise for (2.2) and together capture the most interesting dynamic effects that we have identified over a range of g_{syn} values. The case $g_{syn} = 1.0$ represents an interesting transitional case between solutions in which v_1 remains relatively steady at a low level and solutions for which v_1 spikes repeatedly. The cases $g_{syn} = 4.1$ and $g_{syn} = 5.1$ are representative of two related yet distinct solution behaviors each seen over a wide range of g_{syn} values.

In the following, we will present analysis from two points of view, one that focuses on the roles of $\mathcal{M}_s$ and $\mathcal{M}_{ss}$ in organizing the flow of the full model and another that focuses on how the oscillations of (v_2, w_2) affect the dynamics of (v_1, w_1). The inclusion of both perspectives, we feel, provides the clearest picture of how the dynamics emerges, and may be of use to those readers who typically adopt only one perspective or the other.

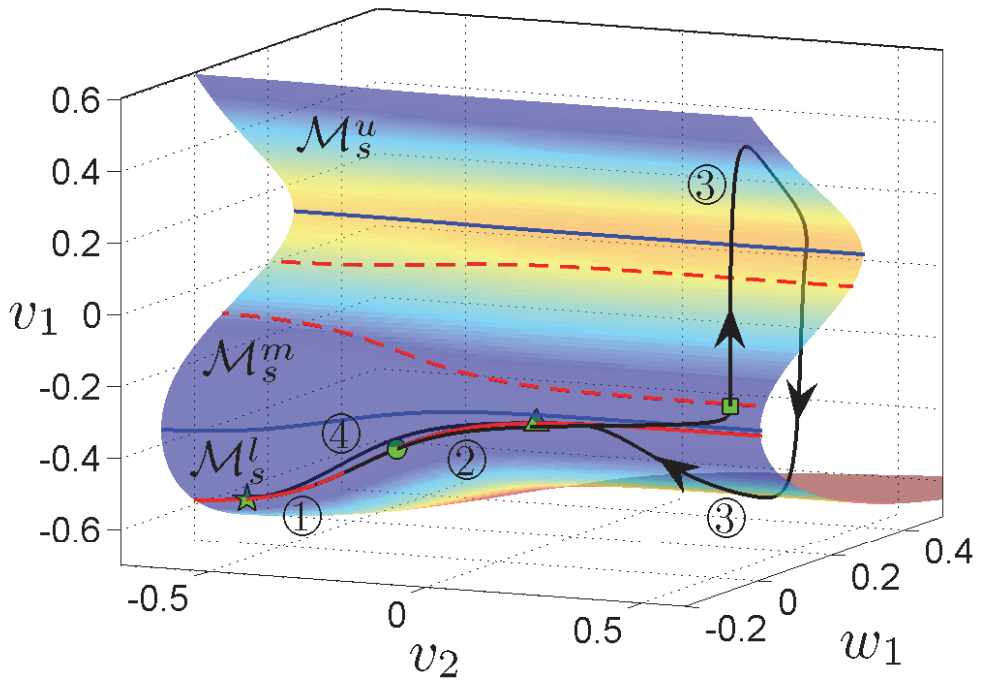

Figure 9. *An attracting solution of (2.2) for $g_{\rm syn} = 1.0$ (black curve), projected to (v_1, w_1, v_2)-space. Also shown are projections of the critical manifold, $\mathcal{M}_s$ (colored surface), and the superslow manifold, $\mathcal{M}_{ss}$ (red curves). The labels $\mathcal{M}_s^u$ and $\mathcal{M}_s^l$ denote, respectively, the upper and lower sheets of $\mathcal{M}_s$, both of which are attracting under the fast flow, while $\mathcal{M}_s^m$ denotes the middle branch of $\mathcal{M}_s$, which is unstable under the fast flow. The coloring on $\mathcal{M}_s$ indicates variation in the w_1-coordinate, with cooler colors for smaller w_1. The blue curves show the folds on $\mathcal{M}_s$. The solid (resp., dashed) red curves are the branches of $\mathcal{M}_{ss}$ that are attracting (resp., repelling) under the slow flow. The green symbols indicate transition points between slow and superslow flow for the (v_2, w_2) oscillator, as shown in Figure 8.*

3.1. Case 1: $g_{\rm syn}$=1.0.

3.1.1. Relation of the trajectory to $\mathcal{M}_s$ and $\mathcal{M}_{ss}$. Figure 9 shows a projection onto (v_1, w_1, v_2)-space of the solution shown in the upper left panel of Figure 2. Also shown in Figure 9 are the projections of $\mathcal{M}_s$ and $\mathcal{M}_{ss}$ onto this space. The critical manifold $\mathcal{M}_s$ has three sheets, $\mathcal{M}_s^l, \mathcal{M}_s^m, \mathcal{M}_s^u$. With respect to the fast layer problem, the outer sheets, $\mathcal{M}_s^u$ and $\mathcal{M}_s^l$, are stable while the middle sheet, $\mathcal{M}_s^m$, is unstable. The green square in Figure 9, which lies just above $\mathcal{M}_s^m$ in the v_1 direction, marks the point where v_2 is maximal, at the start of phase ③ in Figure 8. From here, the trajectory (black curve) evolves on $\mathcal{M}_\sigma$ (not shown). Initially, the solution follows the fast flow (2.6) towards $\mathcal{M}_s^u \cap \mathcal{M}_\sigma$, then evolves along $\mathcal{M}_s^u \cap \mathcal{M}_\sigma$ under (2.16) until it reaches the upper fold of $\mathcal{M}_s$ (upper blue curve, Figure 9), from which it jumps under (2.6) towards $\mathcal{M}_s^l$. Within $\mathcal{M}_s^l$, we observe that the trajectory is attracted to a branch of the superslow manifold $\mathcal{M}_{ss}$, making a long excursion on $\mathcal{M}_s^l$, again under (2.16), towards and then along $\mathcal{M}_{ss}$ (solid red curve, Figure 9). Note that there are also two branches of $\mathcal{M}_{ss}$ on $\mathcal{M}_s^m$ (dashed red curves, Figure 9), but these do not influence

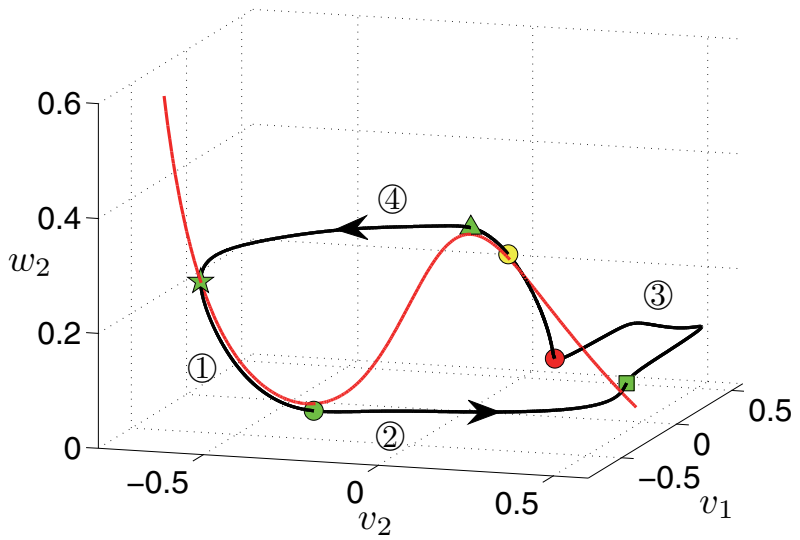

Figure 10. *Projection of the solution from Figure 9 to (v_1, v_2, w_2)-space. Also shown is $\mathcal{M}_{ss}$ (red curve). The solution trajectory (black curve) reaches $\mathcal{M}_s^l$ at the red dot and is attracted by a stable part of $\mathcal{M}_{ss}$, which it starts following under (2.13) near the yellow dot. Green symbols are as in Figure 8.*

the dynamics of interest here.

Further insight into the dynamics on $\mathcal{M}_s^l$ comes from viewing the trajectory in (v_1, v_2, w_2)-space, as in Figure 10. When the trajectory reaches $\mathcal{M}_s^l$ (red dot in Figure 10) during phase ③ of the (v_2, w_2) cycle, it is governed by (2.16), for which a branch of $\mathcal{M}_{ss}$ is attracting (red curve). The trajectory approaches $\mathcal{M}_{ss}$ and then moves along it (approximately from the yellow dot) under the superslow reduced flow (2.13) until it reaches the fold of $\mathcal{M}_{ss}$ (green triangle), from which it jumps under (2.10). This jump (phase ④) takes the trajectory away from $\mathcal{M}_\sigma$ but it remains within $\mathcal{M}_s^l$ and asymptotes to another stable branch of $\mathcal{M}_{ss}$ in $\mathcal{M}_\sigma \cap \mathcal{M}_s^l$. The solution then moves under (2.13), following the second stable branch of $\mathcal{M}_{ss}$ in the direction of decreasing w_2 (phase ①) until it reaches the next fold of $\mathcal{M}_{ss}$ and starts to jump back to large v_2, again under (2.10). However, as the solution approaches the other branch of $\mathcal{M}_{ss}$ (near the green square; see also Figure 9), it crosses the lower fold of $\mathcal{M}_s$ and jumps again, this time under the fast flow (2.6), towards $\mathcal{M}_s^u$, from which point the previous paragraph applies.

The above discussion reveals how the three time scales influence the solution. The v_2 and w_2 variables always evolve on the slow or superslow time scale, but the speeds of v_1 and w_1 depend on the phase of the oscillation. In particular, the jumps between sheets of $\mathcal{M}_s$ are fast, and the excursions along $\mathcal{M}_s$ that follow are slow, except for when the trajectory is in a neighborhood of a stable part of $\mathcal{M}_{ss}$ within $\mathcal{M}_s^l$, in which case the superslow time scale emerges. This behavior is consistent with what is expected from GSPT analysis applied to two-time-scale systems; at each instant in time, the dynamics is governed by the fastest time scale system that has not converged to an attracting limit.

Implicit in this discussion is that in the singular limit the trajectory always meets the fold

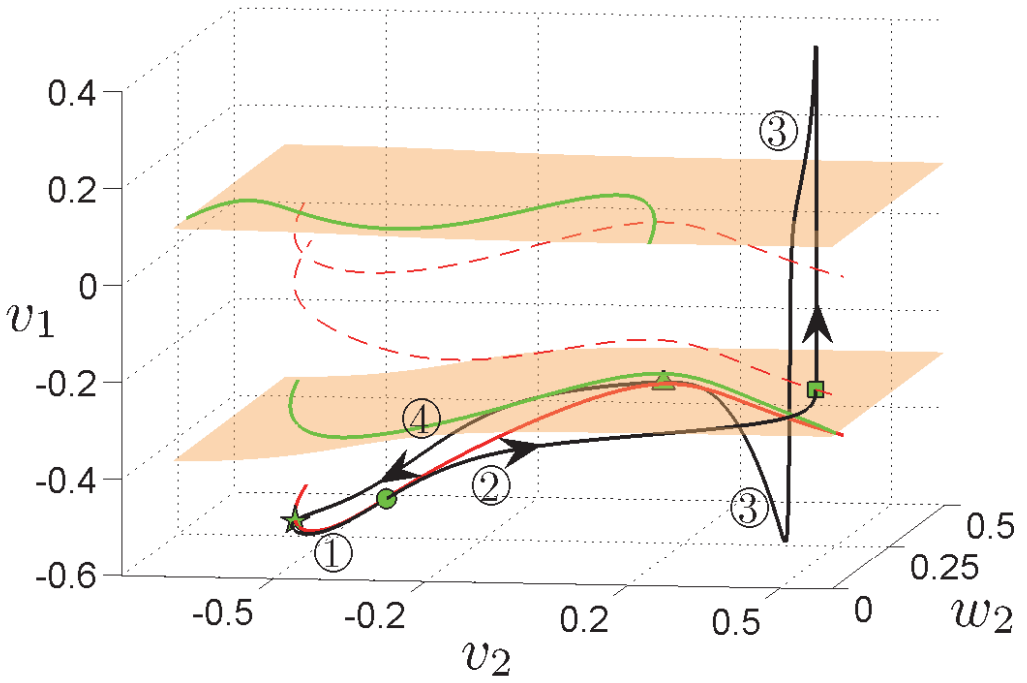

Figure 11. *Projection to (v_1, v_2, w_2)-space of the surfaces of folds of $\mathcal{M}_s$ (orange), the superslow manifold $\mathcal{M}_{ss}$ (red), the folded singularities (green), and the attracting solution (black), for $g_{\text{syn}} = 1.0$. The red curves are the same branches of $\mathcal{M}_{ss}$ shown in Figure 10; note that the solid red curve lies within $\mathcal{M}_s^l$ and remains below the lower fold surface (see Figure 9). The solution trajectory crosses each fold surface a significant distance from the curves of folded singularities.*

surface of $\mathcal{M}_s$ at a jump point. Figure 9 does not capture the structure of the fold surfaces, but they can be visualized in (v_1, v_2, w_2)-space; see Figure 11. The trajectory actually crosses each fold surface only once per cycle: it crosses the lower fold surface with v_1 increasing just before it reaches the green square and crosses the upper fold surface with v_1 decreasing to the left of and above the rightmost black arrow head. The two other apparent crossings of the fold surfaces are artifacts of the projection used. Also shown in Figure 11 are the curves of folded singularities, computed using (2.21). Importantly, note that the trajectory always crosses the fold surfaces at normal jump points, significantly distant from the folded singularities, and thus the folded singularities do not appear to play a significant role in the dynamics.

3.1.2. (v_1, w_1) driven by (v_2, w_2). We now consider (1.1) from the perspective of a fast-slow system driven by a slow-superslow oscillation. The use of this kind of perspective has proved helpful in past analyses of various models with two time scales (e.g., [28, 27, 25, 24, 3]).

Recall that for the parameter values we are considering, in the absence of coupling, the (v_1, w_1) system has a stable equilibrium but no oscillatory solution. If coupling is introduced by setting $g_{syn} = 1.0$, however, then oscillations in v_1 are observed, as can be seen in Figure 2. It might be natural to ascribe the onset of these oscillations to variation of v_2 pushing the v_2-frozen system (2.17) through a bifurcation at which oscillations are born. As shown in

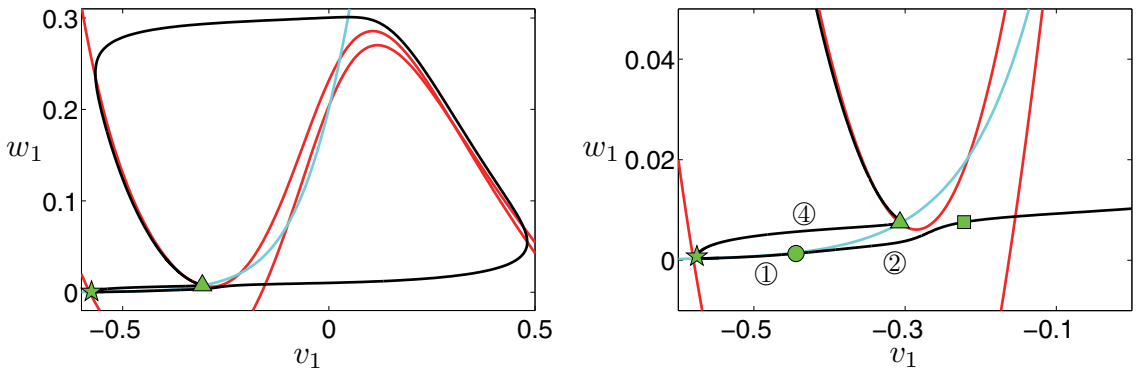

Figure 12. *The attracting trajectory from Figure 9 (black curve) projected to the (v_1, w_1) plane; the right panel shows an enlargement of part of the left panel. Circled numbers and green symbols correspond to phases of the (v_2, w_2) oscillation and the transition points, as shown in Figure 8. The cyan curve is the w_1-nullcline for (2.17), which is independent of v_2, while the red curves are the v_1-nullclines for (2.17) for $v_2 = v_{2_{max}}$ (higher red curve) and $v_2 = v_{2_{min}}$ (lower red curve).*

Figures 5 and 6, however, there is no such bifurcation for $g_{syn} = 1.0$. The key point in considering the dynamics with $g_{syn} = 1.0$ from the perspective of (v_2, w_2) driving (v_1, w_1) is to explain the observed oscillations in v_1.

To provide this explanation, we consider the phases of the (v_2, w_2) oscillation in succession. The yellow dot in Figure 10 marks the point in phase ③ where the conditions $f_1 = g_1 = f_2 = 0$ become (approximately) satisfied; the trajectory at this point lies on the v_2-nullcline when projected to the (v_2, w_2) plane and at the intersection of the v_1- and w_1-nullclines of the v_2-frozen system (2.17) when projected to the (v_1, w_1) plane. From the yellow dot, the solution evolves under the superslow reduced problem (2.13) with v_2 slaved to w_2. The evolution of v_2 in turn moves the v_1-nullcline of (2.17) on the superslow time scale, while the w_1-nullcline is independent of v_2 and thus remains fixed. The (v_1, w_1) projection of the trajectory then tracks the intersection of the v_1- and w_1-nullclines. In fact, $v_2 > 0$ throughout phase ③, so based on the shape of $S(v_2)$, which provides the coupling from v_2 to v_1, these intersection points depend only very weakly on v_2 (see Figure 7). Thus, if projected to the (v_1, w_1) plane, the yellow dot would lie almost on the green triangle that marks the end of phase ③, and the trajectory remains near the green triangle throughout this part of phase ③ (Figure 12).

After the trajectory passes the green triangle and moves into phase ④, the condition $f_2 = 0$ no longer applies. The flow is now governed by the slow reduced layer problem (2.10). The trajectory still lies on $\mathcal{M}_s$, and thus, in the projection to the (v_1, w_1) plane, is on the curve $f_1(v_1, w_1, v_2) = 0$, but it diverges from the w_1-nullcline (cyan curve in Figure 12). Correspondingly, the trajectory diverges from the red curve in Figure 13, which shows the w_1-coordinate of the intersection of v_1- and w_1-nullclines of (2.17) for each v_2.

Phase ④ ends when the trajectory converges to a critical point of (2.10), at which time its projection to the (v_2, w_2) plane reaches the left branch of the v_2-nullcline. The v_2-coordinate of this point is the minimal value of v_2 along the trajectory; call it $v_{2_{min}}$. Within the (v_1, w_1) plane, the trajectory is seen to converge to a point at the intersection of the v_1- and w_1-

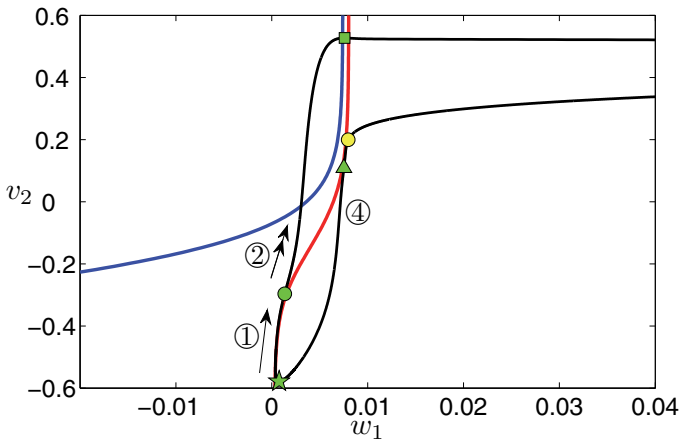

Figure 13. *The attracting trajectory from Figure 9 (black curve) projected onto the (w_1, v_2) plane. Circled numbers and green symbols correspond to phases of the (v_2, w_2) oscillation and their transition points as in Figure 8. The yellow dot indicates where the trajectory reaches a small neighborhood of a critical point of the slow reduced layer problem on $\mathcal{M}_\sigma$, namely, a point of $\mathcal{M}_{ss}$ within $\mathcal{M}_s^l$, as in Figure 10. The blue curve shows the w_1-coordinate of the left fold of the v_1-nullcline for (2.17), while the red curve indicates the w_1-coordinate of the intersection of the v_1- and w_1-nullclines for (2.17), both parametrized by v_2. The direction of flow on the trajectory is indicated by arrows, one arrowhead for superslow flow and two for slow flow.*

nullclines for the v_2-frozen system (2.17), with the v_1-nullcline computed with $v_2 = v_{2_{min}}$ (green star in Figure 12). This convergence corresponds to the end of the jump between branches of $\mathcal{M}_{ss}$ within $\mathcal{M}_s^l$ described in the previous subsection.

Next, phase ① is governed by the superslow reduced flow (2.13), as for phase ③. Under this flow, the v_1-nullcline for (2.17) moves superslowly in the (v_1, w_1) plane, while the w_1-nullcline stays fixed, and the projection of the trajectory tracks the fixed point of (2.17) along the w_1-nullcline (green star to green circle in Figures 12–13). Since there is no bifurcation in (2.17) as v_2 varies, this situation continues until the trajectory reaches the lower fold of the v_2-nullcline in the (v_2, w_2) plane, as marked by the green circle, at the end of phase ①.

The most interesting phase of this oscillation is phase ②. At the start of this phase (green circle in Figures 12 and 13), the trajectory is governed by (2.10) and v_2 begins a slow jump away from its nullcline. During this slow jump, v_1 is slaved to w_1 and v_2, as in phase ④. Even though (2.17) does not govern the evolution of this part of the trajectory, it is still useful to track the v_1-nullcline of (2.17), which slowly slides in the direction of increasing w_1 in the (v_1, w_1) plane. Each such nullcline has two folds; as can be seen in Figure 13, the slow flow of (2.10) steers the trajectory across the one-dimensional curve of lower folds of the family of v_1-nullclines (blue curve), projected to the (w_1, v_2) space. Thus, we observe that the flow of (2.10), in which the two slow variables conspire to pull the trajectory away from the curve of fixed points of (2.17) and across the curve of lower folds of the family of v_1-nullclines, is crucial for the emergence of an oscillation in v_1 for $g_{syn} = 1.0$.

Following the fold crossing, there is a fast jump in v_1 governed by (2.6), from left to right branches of the v_1-nullcline family in the projection to the (v_1, w_1) plane. If we had a greater

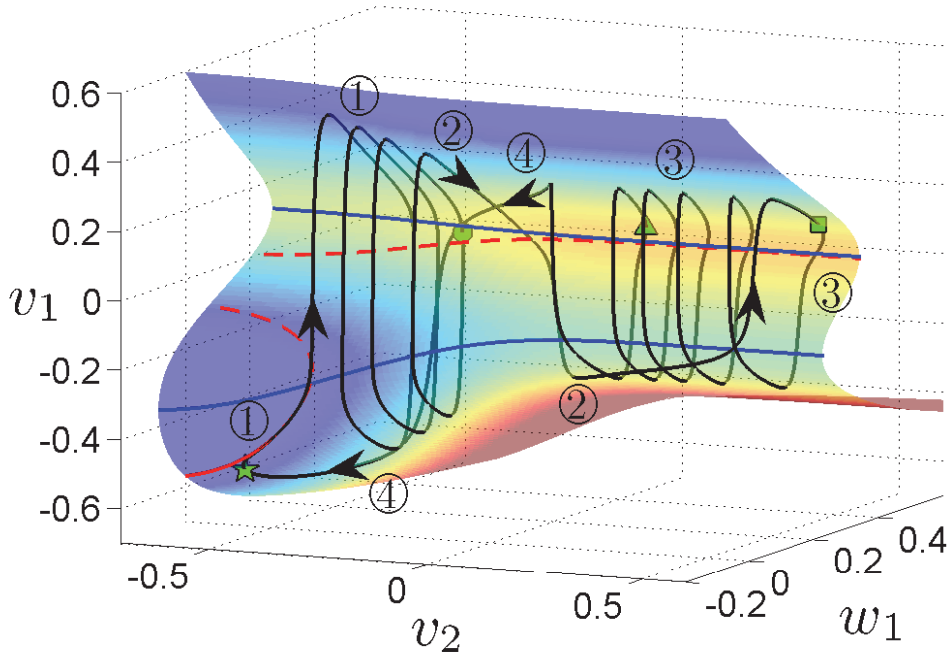

Figure 14. *An attracting solution of (2.2) for $g_{\rm syn} = 4.1$, projected to (v_1, w_1, v_2)-space (black curve). Also shown are projections of $\mathcal{M}_s$ (colored to indicate variation in w_1), the folds of $\mathcal{M}_s$ (blue curves), and $\mathcal{M}_{ss}$ (red curves, solid where attracting, dashed otherwise). The green symbols indicate transition points between slow and superslow flow for the (v_2, w_2) oscillator, as shown in Figure 8.*

separation of time scales, then the jump would occur almost as soon as the fold was crossed. With the weaker separation that we consider, the jump is delayed; it begins quite close to the end of phase ② and ends during phase ③ (Figure 12, right panel). Once the jump in v_1 is complete, just after the start of phase ③, the trajectory evolves under (2.16) or, equivalently, under the reduced problem for (2.17), tracking the right branches of the v_1-nullclines in the direction of increasing w_1 in the projection to the (v_1, w_1) plane (Figures 12 (left) and 13). The trajectory eventually reaches the right knee curve of the v_1-nullcline family and jumps down to the left v_1-nullcline branches (red dot in Figure 10) under (2.6) or, equivalently, under the layer problem of (2.17). Finally, the trajectory converges under (2.16) to the curve of critical points where the v_1-nullclines intersect the w_1-nullcline (yellow dot in Figure 13), bringing us back to where we started our description.

Remark 3.1. *In the true singular limit, we expect that the fast jump up of v_1 would happen instantly with respect to the slow time scale, during phase ②. After that jump, w_1 and v_2 would evolve according to (2.10), continuing phase ②, until being interrupted again by the fast jump down of v_1. Finally, the slow evolution of (2.10) would continue until convergence to where $f_1 = g_1 = f_2 = 0$, analogous to our yellow dot point, at the end of phase ②. This progression is expected from GSPT, and we have observed it numerically (not shown).*

3.2. Case 2: $g_{\rm syn}$=4.1.

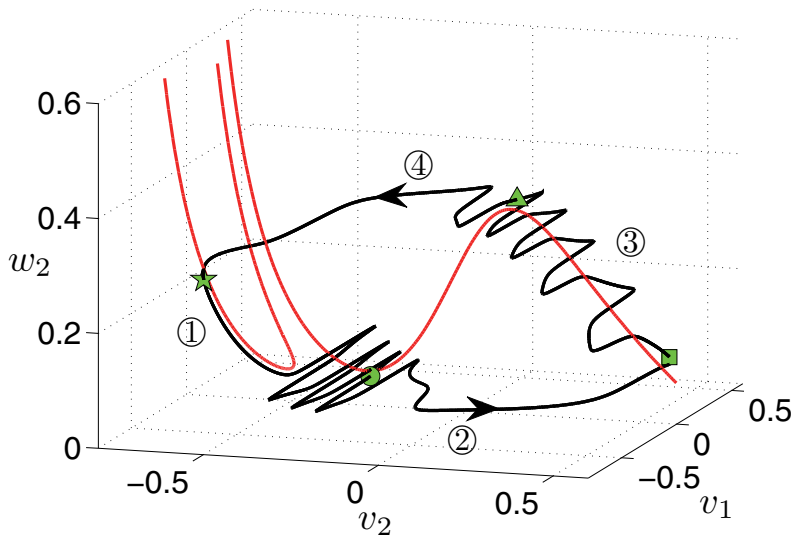

Figure 15. *The solution from Figure 14 projected to (v_1, v_2, w_2)-space (black curve). Also shown is $\mathcal{M}_{ss}$ (red curve). Symbols all have the same meaning as in Figure 8.*

3.2.1. Relation of trajectory to $\mathcal{M}_s$ and $\mathcal{M}_{ss}$. The solution corresponding to the upper right panel of Figure 2 appears in Figure 14 projected onto (v_1, w_1, v_2)-space. Also shown are the projections of $\mathcal{M}_s$ and $\mathcal{M}_{ss}$ onto this space. Figure 15 shows a different projection of the same solution, this time onto the (v_1, v_2, w_2)-space. When $g_{syn} = 1.0$, there were three branches of $\mathcal{M}_{ss}$ within $\mathcal{M}_s$, each extending over all values of v_2 (Figure 9). When $g_{\text{syn}} = 4.1$, however, only one branch of $\mathcal{M}_{ss}$ (on the middle branch of $\mathcal{M}_s$) extends to all values of v_2, with the other branches being replaced by a single curve that intersects both the lower and middle sheets of $\mathcal{M}_s$; see Figure 14.

The evolution of the attracting orbit in this case can be understood in terms of the shapes and relative positions of $\mathcal{M}_s$ and $\mathcal{M}_{ss}$. Starting from the green star in Figure 14, the trajectory is in phase ① and evolves on the superslow time scale under (2.13). It follows $\mathcal{M}_{ss}$ to the lower fold of $\mathcal{M}_s$, where it makes a jump to $\mathcal{M}_s^u$ on the fast time scale under (2.6); this jump corresponds to the onset of spikes in v_1. Since there are no branches of $\mathcal{M}_{ss}$ on $\mathcal{M}_s^u$, the trajectory moves on the slow time scale along $\mathcal{M}_s^u \cap \mathcal{M}_\sigma$ under (2.16) until it meets the upper fold, from which it jumps back to $\mathcal{M}_s^l$ under (2.6). Now the orbit has reached a part of $\mathcal{M}_s^l$ where there is no nearby branch of $\mathcal{M}_{ss}$ (Figures 14 and 15) and so it moves along $\mathcal{M}_s^l$ under (2.16) until it again reaches the lower fold of $\mathcal{M}_s$. Several more oscillations consisting of fast jumps interspersed with slow segments follow, during which v_2 increases on the superslow time scale; the full three-time-scale evolution occurring here is described by (2.15).

Eventually the trajectory reaches the green circle at the start of phase ②, at which point the speed of evolution of v_2 changes from superslow to slow (see Figure 8). From there, the orbit evolves under (2.11), with alternating fast v_1 jumps (governed by (2.6) in the singular limit) and slow drift (governed by (2.10) in the singular limit). When the green square is reached, phase ③ begins and v_2 once again becomes superslow (see Figures 8 and 15), this

time causing v_2 to decrease. Since there are no branches of $\mathcal{M}_{ss}$ nearby, the orbit continues to make fast-slow loops as v_2 decreases on the superslow time scale until the green triangle is reached. There, phase ④ begins and the oscillatory dynamics is similar to phase ②. Eventually v_2 is sufficiently negative that a fast jump takes the orbit to a region of $\mathcal{M}_s^l$ where there is a nearby branch of $\mathcal{M}_{ss}$. Then the orbit is attracted to $\mathcal{M}_{ss}$ under (2.10) and returns to the green star.

In the description above, it is again implicit that the orbit meets the folds of $\mathcal{M}_s$ at regular jump points. It is straightforward to check that, except for one case, intersections of the attracting orbit with the fold surfaces are relatively far from the curves of folded singularities. The exceptional case is when the orbit jumps at the point where $\mathcal{M}_{ss}$ crosses the lower fold of $\mathcal{M}_s$. The intersection of a branch of $\mathcal{M}_{ss}$ and a fold of $\mathcal{M}_s$ must always be a folded singularity, since $g_1(v_1, w_1) = f_2(v_2, w_2) = 0$ on $\mathcal{M}_{ss}$ and so condition (2.21) is satisfied. A complete unfolding of this type of folded singularity has not, to our knowledge, been performed, although [31] discusses some features of this type of singularity in a specific system and shows that subthreshold oscillations are associated with passage near the folded singularity of that system. In our case, numerical results suggest that orbits that follow $\mathcal{M}_{ss}$ to the folded singularity at the fold of $\mathcal{M}_s$ make a regular jump, and it appears that no complicated dynamics are induced by the folded singularity. A proper investigation of this type of singularity is left for future work.

3.2.2. (v_1, w_1) driven by (v_2, w_2). We now use our alternative perspective to explain properties of the attracting solution when $g_{\text{syn}} = 4.1$. Figure 5 shows that treating v_2 as a parameter in the v_2-frozen system (2.17) and increasing v_2 from its minimal relevant value pushes (2.17) through a homoclinic bifurcation, resulting in the appearance of oscillatory solutions of (2.17); these oscillations persist no matter how large v_2 becomes, which explains why the v_1 spikes continue throughout phase ③ as v_2 drifts on the superslow time scale and only end after v_2 drops below the homoclinic bifurcation value during phase ④.

Next, we explain why the amplitude of the v_1 spikes decreases progressively during phase ① until v_2 jumps up in phase ②, and then remains approximately constant throughout phase ③. Consider the effect of v_2 on the position of the v_1-nullcline of (2.17). At the start of phase ① the v_1- and w_1-nullclines intersect in three critical points (Figure 16, lowest red curve and cyan curve). Under (2.15), as v_2 increases on the superslow time scale during phase ①, it raises the corresponding v_1-nullcline of (2.17). This rise is not uniform in v_1, however; since it occurs through the term $g_{syn}S(v_2)(v_1 - V_{syn})$ in (1.1), a fixed change in v_2 causes a relatively large change in the w_1-values along the part of the v_1-nullcline with v_1 far below V_{syn}, including the left branch of the v_1-nullcline, and a relatively small change where $|v_1 - V_{syn}|$ is small, including the right branch of the v_1-nullcline (Figure 16).

The increase in v_2 causes a bifurcation in which two of (v_1, w_1) critical points near the left knee of the v_1-nullcline, with v_1 values far from V_{syn}, merge and annihilate. For each v_2 above the bifurcation value, (2.17) exhibits a stable relaxation oscillation involving fast jumps in v_1 between branches of the v_1-nullcline alternating with slow drift in (v_1, w_1) along these branches. Since the right branch of the nullcline depends little on v_2, each jump down occurs from a similar value of w_1 even as v_2 varies (Figure 16). The minimal values of v_1 within spikes are determined by the fast flow and increase with v_2, since they are on the left branches of the

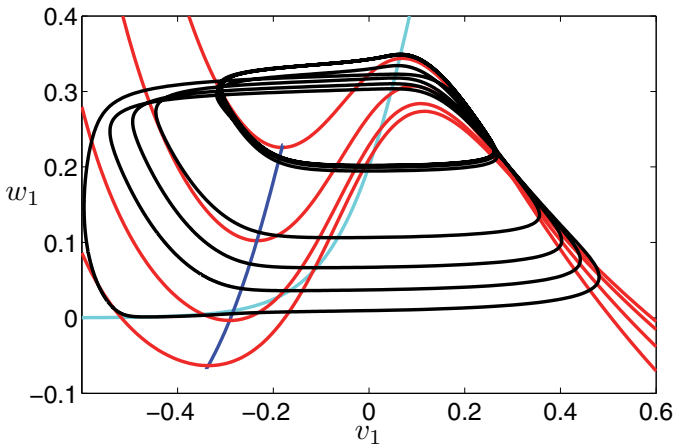

Figure 16. *Nullclines for (2.17) for the case $g_{syn} = 4.1$. The red curves are v_1-nullclines for a selection of fixed values of v_2; these move upward as v_2 increases. The cyan curve is the w_1-nullcline, which is independent of v_2, and the blue curve denotes the left folds of the v_1-nullclines over the full range of v_2 arising during v_2 oscillations. The black curve is a projection of the periodic orbit shown in Figure 14.*

v_1-nullclines. Thus, we find increasing v_1 values along successive v_1 spike troughs before v_2 becomes active. Furthermore, the jumps up in v_1 occur from larger w_1 values across successive spikes as v_2 increases. These jumps land at points on similar negatively sloped right branches, meaning that an increase in w_1 translates to a decrease in v_1 at the landing point (Figure 16). Thus, peak values of v_1 decrease across successive spikes during this phase.

When phase ① ends, v_2 jumps up through and beyond the active range of $S(v_2)$ (Figure 7) to the right branch of its nullcline in the (v_2, w_2) phase plane, where phase ③ begins. The (v_1, w_1) relaxation oscillations continue; since $S(v_2)$ remains approximately constant, so does the v_1-nullcline and hence so do the quantitative features of the relaxation oscillation. The insensitivity of the v_1 equation to v_2 in phase ③ explains why the v_1 spikes have approximately constant amplitude throughout this phase (upper right cycles in the trajectory in Figure 16).

The discussion above shows how variations in v_2 can shape the v_1 spikes: superslow drift in v_2 imposes a superslow v_1 spike amplitude modulation. To appreciate fully how transitions in the v_2 dynamics relate to the (v_1, w_1) dynamics, we consider the projection of the attracting solution onto the (w_1, v_2) plane (see Figure 17). During the part of phase ① when there is no spiking, the trajectory evolves under (2.13), moving along an attracting branch of $\mathcal{M}_{ss}$ (near the single arrow). A fast excursion away from $\mathcal{M}_{ss}$, and in fact away from $\mathcal{M}_s$ altogether, occurs when the branch of $\mathcal{M}_{ss}$ crosses the fold of $\mathcal{M}_s$ (green diamond). At the onset of the fast jump, v_2 is still below the value corresponding to the left fold of the v_2-nullcline and continues to drift on the superslow time scale, while the (v_1, w_1) system has alternating fast and slow segments, with w_1 oscillating between the folds of the v_1-nullcline (blue curves), under (2.15). Once the lower fold of the v_2-nullcline is crossed (green circle), (2.10) governs the slow segments of the trajectory; these alternate with fast jumps governed by (2.6), but there is only time for a few of these jumps, since w_1 and v_2 evolve on the same time scale during

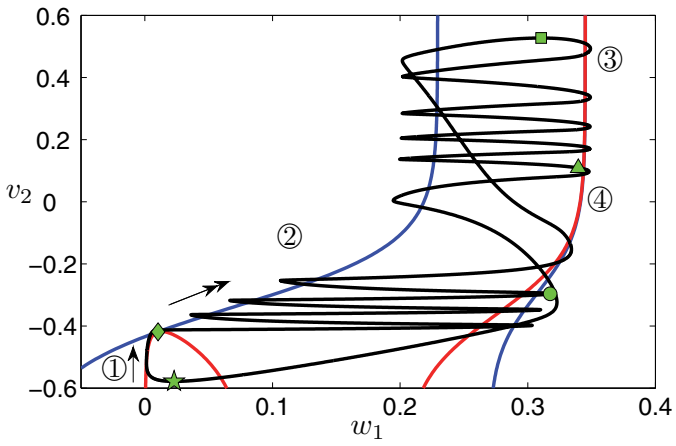

Figure 17. *Projection to the (w_1, v_2) plane illuminates several features of the periodic solution (black) for $g_{syn} = 4.1$. The red curves are branches of $\mathcal{M}_{ss}$ or, equivalently, critical points of (2.17), the blue curves are the left (smaller w_1) and right (larger w_1) folds of the v_1-nullcline, the green diamond marks the time point when v_1 begins spiking, and the other green symbols have the same meanings as in Figure 8.*

this phase. The return of (v_2, w_2) to a neighborhood of the v_2-nullcline occurs as v_2 reaches its maximum value (green square); then the evolution of v_2 becomes superslow again, so that only small decreases in v_2 are seen during the subsequent spikes governed by (2.17). This progression continues until (v_2, w_2) crosses the right fold of the v_2-nullcline (green triangle), at which time another slow jump in v_2 occurs. Under (2.10), the trajectory then converges back to $\mathcal{M}_{ss}$, completing the cycle.

Figure 17 shows clearly the v_2-dependence of the w_1 coordinate on folds of the v_1-nullcline of (2.17), as discussed earlier. The w_1 coordinate of the left folds of the v_1-nullcline depends strongly on v_2 while v_2 is negative but becomes approximately independent of v_2 at positive v_2, while the w_1 coordinate of the right folds is more weakly dependent on v_2 and also becomes approximately independent of v_2 for v_2 sufficiently large (Figure 17). Correspondingly, the minimal w_1 value during a spike increases on subsequent spikes when the (v_2, w_2) system is in phase ①, as does the minimal v_1 value, and is approximately constant when the (v_2, w_2) system is in phase ③. The maximal w_1 value remains relatively constant over all spikes.

3.3. Case 3: $g_{syn} = 5.1$.

3.3.1. Relation of the trajectory to $\mathcal{M}_s$ and $\mathcal{M}_{ss}$. A key new feature that arises for $g_{syn} = 5.1$ is that a branch of $\mathcal{M}_{ss}$ crosses from the middle to the upper sheet of $\mathcal{M}_s$ as v_2 increases (Figure 18). Thus, while the behavior of the orbit during phase ①, from the green star to the green circle, is quite similar to that seen when $g_{syn} = 4.1$, qualitatively different behavior arises after that. In particular, after passing the green circle and starting phase ②, the orbit undergoes one more fast-slow oscillation in (v_1, w_1, v_2), governed by (2.11), and then settles on $\mathcal{M}_s^u$, where it evolves towards the fold curve of $\mathcal{M}_s$ under (2.10). Once the green square is reached and phase ③ begins, the orbit follows an attracting branch of $\mathcal{M}_{ss}$ under (2.13) until the green triangle is reached and phase ④ starts. Then v_2 starts to decrease at a

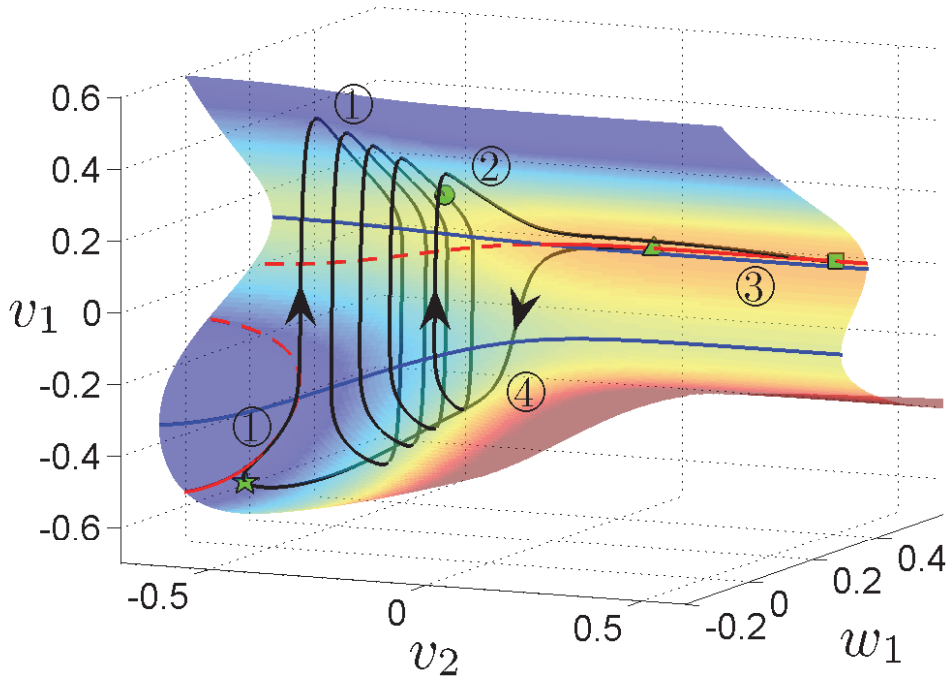

Figure 18. *An attracting solution of (2.2) for $g_{\mathrm{syn}} = 5.1$, projected to (v_1, w_1, v_2)-space (black curve). Also shown are projections of $\mathcal{M}_s$ (colored to indicate variation in w_1), the folds of $\mathcal{M}_s$ (blue curves), and $\mathcal{M}_{ss}$ (red curves, solid where attracting, dashed otherwise). The green symbols indicate transition points between slow and superslow flow for the (v_2, w_2) oscillator, as shown in Figure 8.*

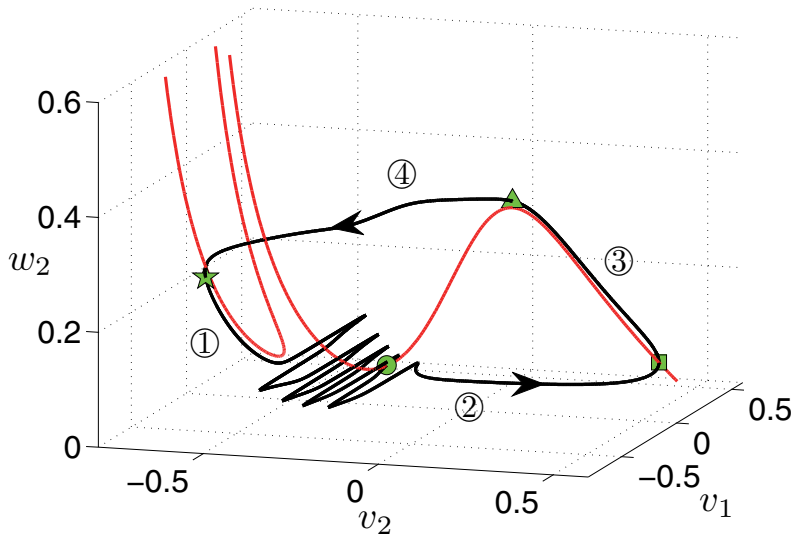

Figure 19. *The solution from Figure 18 projected onto (v_1, v_2, w_2)-space. $\mathcal{M}_{ss}$ is also shown (red curve). Symbols all have the same meanings as in Figure 8.*

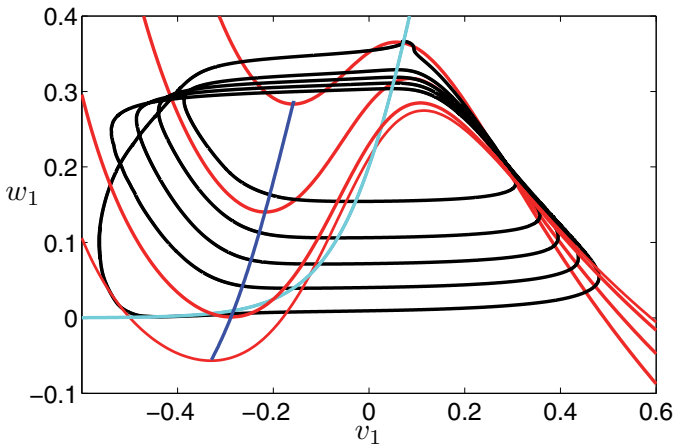

Figure 20. *Nullclines for (2.17) for the case $g_{syn} = 5.1$. The black curve is a projection of the periodic orbit shown in Figure 18. Colors of curves are as in Figure 16.*

greater rate (on the slow time scale), attempting to jump to another attracting branch of $\mathcal{M}_{ss}$ (left branch of the cubic shaped section of $\mathcal{M}_{ss}$ in Figure 19). Although this flow is governed by (2.10), $g_2 \approx 0$ and hence little change in w_1 occurs. Before the other branch of $\mathcal{M}_{ss}$ is reached, the orbit encounters the fold surface for $\mathcal{M}_s$ and then jumps in v_1 under the fast flow of (2.6) and returns to $\mathcal{M}_s^l$ near the green star, completing one period of the oscillation.

Just as for the case of $g_{syn} = 4.1$, it can be checked that folded singularities do not have a role in the dynamics. Again, there is a folded singularity at the intersection of the fold of $\mathcal{M}_s$ and the lower branch of $\mathcal{M}_{ss}$, but as with $g_{syn} = 4.1$, the orbit appears to make a straightforward fast jump at this point. There is also a folded singularity where the branch of $\mathcal{M}_{ss}$ hits the upper fold of $\mathcal{M}_s$, but the orbit leaves $\mathcal{M}_{ss}$ before reaching the fold of $\mathcal{M}_s$ so this folded singularity is not relevant to the observed dynamics.

3.3.2. (v_1, w_1) driven by (v_2, w_2). Comparing the relevant bifurcation diagrams in Figure 5 shows that changes in v_2 have a qualitatively similar impact on the v_2-frozen system (2.17) for $g_{syn} = 5.1$ as for $g_{syn} = 4.1$ except that for $g_{syn} = 5.1$, when v_2 becomes sufficiently large, oscillations of (2.17) are lost as a stable critical point at elevated v_1 is born through an AH bifurcation. Correspondingly, comparing Figures 20 and 16 reveals a similar progression of v_1-nullclines except that when $g_{syn} = 5.1$, the upper knee of the v_1-nullcline eventually crosses the w_1-nullcline, so that the w_1-nullcline intersects the uppermost v_1-nullcline on its right branch. The trajectory tends towards this intersection point on the slow time scale during phase ② and remains in a small neighborhood of the point throughout phase ③.

Similarly, there is a strong resemblance between the slow phase plane projections in Figures 21 and 17. The key new feature that arises for $g_{syn} = 5.1$ is that there is an attracting limit point of (2.10) at the green square in Figure 21. This point becomes attracting because the curve of critical points of (2.17) (red) crosses through the fold curve (blue) with increasing v_2; due to the projection, the crossing appears as a tangency in Figure 21 (green diamond). After the trajectory reaches the green square, it drifts back down the red curve on the superslow

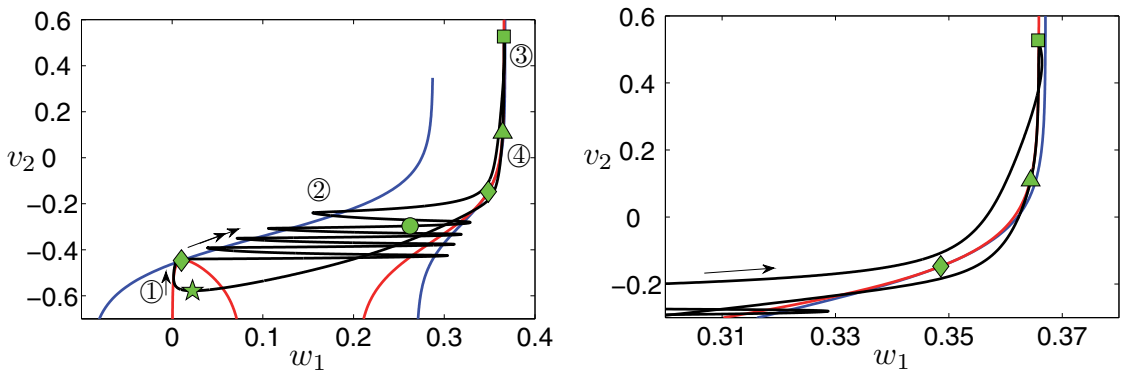

Figure 21. *Projection to the (w_1, v_2) plane illuminates several features of the periodic solution (black) for $g_{syn} = 5.1$. Color coding and symbols have the same meaning as in Figure 17, except there is now a diamond appearing on the upper (larger w_1) branch of $\mathcal{M}_{ss}$, corresponding to the location of an AH bifurcation in the frozen system (2.17) with v_2 treated as a parameter. Right panel shows an enlarged view.*

time scale under (2.13) until it returns to the fold line (green square to green triangle) and then departs from the nullcline intersection curve on the slow time scale, again under (2.13), converging towards the lower stable branch of $\mathcal{M}_{ss}$.

Importantly, as noted in the previous subsection, the convergence to the limit point on the upper branch of $\mathcal{M}_{ss}$ occurs on the slow time scale, governed by (2.10). That is, while v_2 evolves along the left branch of the v_2-nullcline on the superslow time scale as part of (2.15), (v_1, w_1) engage in fast-slow relaxation oscillations as described by their equations, which comprise (2.17). Once v_2 reaches the lower fold of the v_2-nullcline, however, there is a transition to a phase of slow flow of (2.10) with $v_1 \approx v_1(w_1, v_2)$ satisfying $f_1(v_1(w_1, v_2), v_2, w_1) = 0$. The linearization of (2.10) about its limit point on $\mathcal{M}_{ss}$ yields an upper triangular matrix with real eigenvalues, which can easily be shown to be negative as expected. Thus, this convergence features a direct transition from v_1 spikes to a v_1 plateau, with no damped oscillations. We shall see later that this property contrasts with features of similar solutions in two-time-scale systems.

4. Identifying three-time-scale features. We next seek to identify which aspects of the solutions discussed above are truly three-time-scale features in some reasonable sense. In this section we find it useful to work with our original dimensional system (1.1), which produces the solutions shown in Figure 2, but for convenience we omit units on the parameter values.

Our approach is to transform (1.1) into certain two-time-scale systems by adjusting system parameters, then consider whether these systems can generate solutions that are similar to the three cases considered in section 3. We will exaggerate the time scale separation in the three-time-scale system, speeding up V_1 by decreasing C_1 from 8 to 0.8 and slowing down w_2 by decreasing ϕ_2 from 0.001 to 0.0001. This amounts to reducing both ϵ_1 and ϵ_2 by a factor of 10, to 0.01 and 0.0053, respectively. In our original scaling and in this exaggerated version, our system has 1 fast, 2 slow, and 1 superslow (1F, 2S, 1SS) variables. There are many ways to regroup time scales to transform this system into a two-time-scale system. One natural approach is to slow down V_1, say by setting $C_1 = 80$, so that it evolves on the same time scale

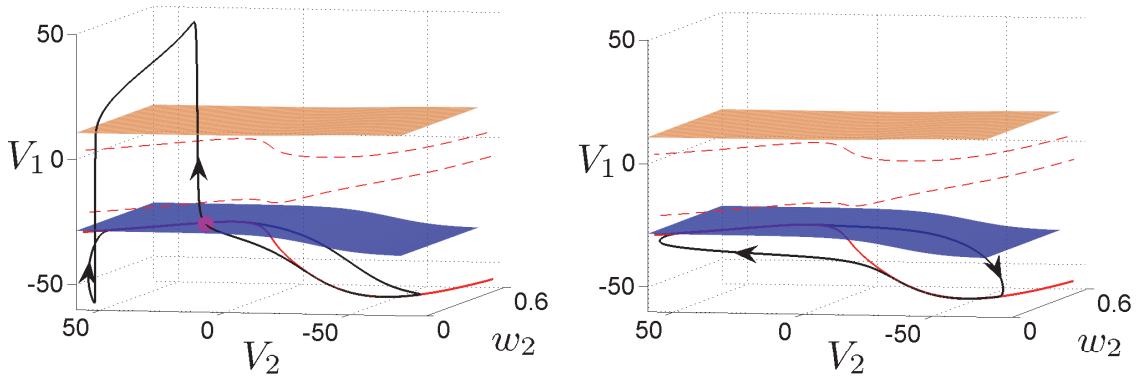

Figure 22. *Projections of solutions for $g_{syn} = 1.0$ onto (V_1, V_2, w_2)-space. The solution trajectory (black curve) exhibits a spike in V_1 for the (1F, 2S, 1SS) system (left) but not for the (3S, 1SS) system (right). In both cases, the red curves are $\mathcal{M}_{ss}$, with stable (unstable) branches drawn as solid (dashed) curves. For the (1F, 2S, 1SS) case, the blue and orange surfaces are folds of $\mathcal{M}_s$. The same surfaces are shown in the (3S, 1SS) case for comparison, although $\mathcal{M}_s$ is no longer meaningful.*

as w_1 and V_2, resulting in a 3 slow, 1 superslow (3S, 1SS) system; similar effects are seen if w_1, V_2, and w_2 are sped up appropriately to produce a system with 3 fast and 1 slow (3F, 1S) variables. Another approach is to speed up w_2, say by increasing ϕ_2 to 0.01, so that it evolves on the same slow time scale as V_2 and w_1, and we have a 1 fast, 3 slow (1F, 3S) system; qualitatively similar effects will be seen for a 1 slow, 3 superslow (1S, 3SS) system obtained by slowing V_1, w_1, and V_2 appropriately. Other rescalings are also possible, leading to pairs of variables on each of two scales, but these require more significant changes, namely, modifying the relative speeds of evolution of two variables or altering the speed of one variable by two orders of magnitude, and so will not be considered.

4.1. $g_{syn} = 1.0$: Recruitment of a transient V_1 spike. When $g_{syn} = 1.0$, (1.1) generates a solution with a single V_1 spike per period, as shown in the first panel of Figure 2. With exaggerated time scale separation, there is little change in this solution. We first compare this solution to solutions from the (3S, 1SS) version of the system (1.1) described above.

Projections onto (V_1, V_2, w_2)-space show that in the (1F, 2S, 1SS) system, the trajectory reaches the lower fold surface of $\mathcal{M}_s$ and jumps to higher V_1. No analogous jump occurs in the (3S, 1SS) case with $g_{syn} = 1.0$ (Figure 22), resulting in an absence of spikes in the V_1 time course (Figure 23, top panel). The fact that (2.17) does not have an AH bifurcation when the frozen variable v_2 is varied can be used to explain why there is no V_1 spike in the (3S, 1SS) case. Consider a trajectory of the (3S, 1SS) system evolving under the superslow flow on the critical manifold for that system, namely, $\mathcal{M}_{ss}$, on a branch where V_1 and V_2 are low. Suppose this trajectory reaches a fold of $\mathcal{M}_{ss}$ such that a transition to the slow layer problem occurs. By construction, the slow layer problem in this case has a unique stable equilibrium point with V_2 high and V_1, w_1 low. The value of V_2 at this equilibrium can be obtained from solving $dV_2/dt_s = 0$ and $\partial(dV_2/dt_s)/\partial V_2 < 0$. The corresponding values of V_1 and w_1 are those for the unique stable equilibrium point of the dimensional version of (2.17) at this V_2 value (see Figure 5). Hence, after passing the fold of $\mathcal{M}_{ss}$, the solution of the (3S, 1SS) system will

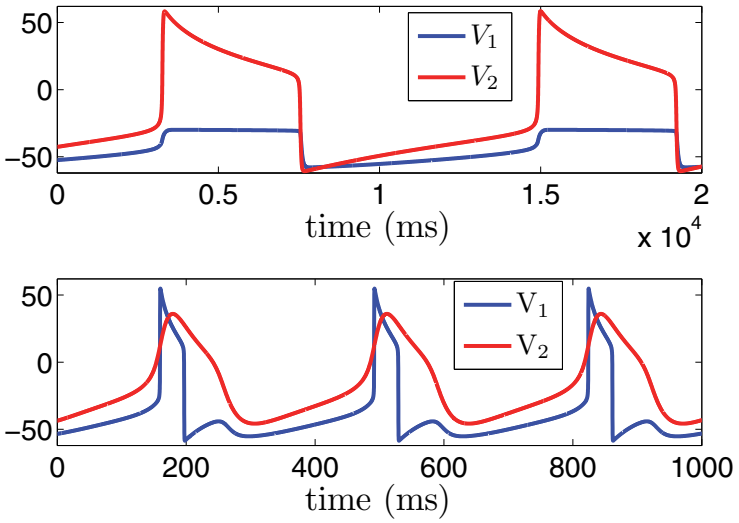

Figure 23. *Time series of rescaled versions of* (1.1) *with* $g_{\rm syn} = 1.0$. *Top: (3S, 1SS) case, with* $C_1 = 80$, $\phi_2 = 0.0001$. *Bottom: (1F, 3S) case, with* $C_1 = 0.8$, $\phi_2 = 0.01$. *Other parameters as in Table 1.*

follow the slow layer flow to the unique stable equilibrium of the layer problem, as seen in the jump from the low-V_2 branch of $\mathcal{M}_{ss}$ to the high-V_2 branch in the right panel of Figure 22. The subsequent motion is governed by the superslow flow, with V_2 slaved to w_2 and (V_1, w_1) following the V_2-dependent branch of stable equilibria until V_2 jumps down again.

The solutions to the (3S, 1SS) case remain similar for all g_{syn} values for which there is no AH bifurcation in (2.17) as v_2 is varied. For g_{syn} fixed sufficiently above the minimal bifurcation value ($\tilde{g}$ from section 2), on the other hand, the trajectory of the (3S, 1SS) system does exhibit a slow V_1 spike after reaching the fold of $\mathcal{M}_{ss}$. These spikes continue even after V_2 reaches the active phase, however. That is, during its active phase, V_2 is slaved to w_2 and hence evolves on the superslow time scale, while the spikes in V_1 (and w_1) occur on the slow time scale and hence occur repeatedly. By continuity, there is a small range of g_{syn} values close to but above $\tilde{g}$ for which very few or even one V_1 spike occurs, but such limited spiking arises because the (V_1, w_1) components of the slow vector field remain quite small beyond the AH bifurcation. Hence, the spikes appear with a significant delay relative to the slow activation of V_2, yielding a qualitatively different solution from that found in the (1F, 2S, 1SS) system with $g_{syn} = 1.0$. Such solutions are straightforward to find numerically but, for reasons of space, we do not show an example here.

Under the alternative rescaling to a (1F, 3S) system, the attracting trajectory with $g_{syn} = 1.0$ is as shown in Figure 23 (bottom). The spike in V_1 has been restored, and the fast jumps in V_1 can be described using the fast flow. However, the solution differs qualitatively from that for the (1F, 2S, 1SS) system (Figure 2). In the (1F, 3S) case, after the initial rise in V_1 under the fast flow, the trajectory is governed by the three-dimensional slow reduced problem along $\mathcal{M}_s^u$. There is no longer a superslow manifold to attract w_1 and V_2, and there is no longer a relaxation oscillation in (V_2, w_2). Thus, the time the trajectory spends on the upper

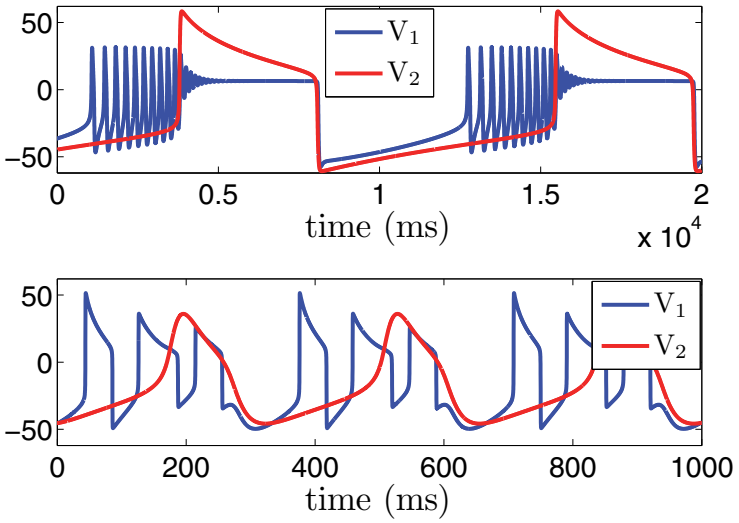

Figure 24. *Time series of* (1.1) *with* $g_{\rm syn} = 4.1$. *Top: (3S, 1SS) case, with* $C_1 = 80$, $\phi_2 = 0.0001$. *Bottom: (1F, 3S) case, with* $C_1 = 0.8$, $\phi_2 = 0.01$. *Other parameters as in Table 1.*

sheet of $\mathcal{M}_s$ (with large V_1) is commensurate with the time for V_2 to fall from higher to lower values, and so the V_1 spike has similar duration to that of V_2. Moreover, after the fast jump down from the upper fold, w_1 continues to evolve along with V_2 and w_2 rather than settling down, and since V_1 is slaved to (w_1, V_2) along $\mathcal{M}_s^l$, there is no longer a prolonged plateau in V_1 after the trough of its spike.

In summary, neither of these two-time-scale systems captures the full features of the oscillating solution shown in the first panel of Figure 2. Since a two-time-scale system will either lose the large spikes in the V_1 time series, generate additional or delayed V_1 spikes, or elongate the V_1 spikes relative to the V_2 spikes and eliminate the plateau in V_1 after each spike, it appears that for (1.1) to produce the solution shown in Figure 2, its three-time-scale structure must be preserved. We therefore classify the solution shown in Figure 2 with $g_{syn} = 1.0$ as an intrinsically three-time-scale phenomenon.

4.2. $g_{syn} = 4.1$: Transition from V_1 spikes of gradually decaying amplitude to V_1 spikes of constant amplitude. When the time scale separation is exaggerated in the (1F, 2S, 1SS) scaling, the qualitative form of the solution with $g_{syn} = 4.1$ does not change, nor does the relevance of the mechanisms shown in Figure 14, although the number of V_1 spikes per cycle increases because the slowed superslow flow prolongs the solution period. In particular, the V_1 time series continues to exhibit two groups of rapid spikes, one with decrementing amplitudes and one with constant amplitudes, corresponding to passage of the trajectory near parts of $\mathcal{M}_s$ with low V_2 (phase ①) and elevated V_2 (phase ③), respectively. With rescaling to (3S, 1SS), the solution time series changes qualitatively (Figure 24, top). In this case, the V_1 spike amplitudes are initially approximately constant, rather than decrementing, then taper off into damped oscillations and approach a plateau, rather than maintaining a fixed amplitude.

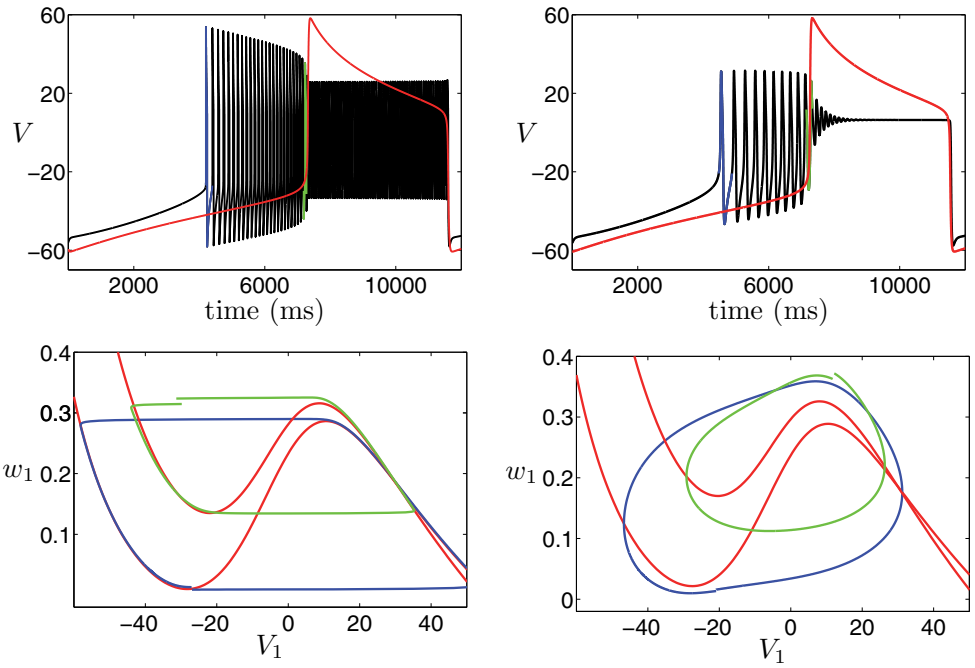

Figure 25. *Top row: Time courses of V_2 (red) and V_1 (black/blue/green) for $C_1 = 0.8$ (left) and $C_1 = 80$ (right), which reduces the amplitude modulation during the period when V_1 is spiking and V_2 is still depressed; $\phi_1 = 0.01$ and $\phi_2 = 0.0001$ in both cases. Bottom row: Projections to the (V_1, w_1) phase plane of the parts of the solutions colored blue and green in the upper row, along with V_1-nullclines computed with V_2 fixed at the value attained by the V_2 time series at the start of the corresponding segment of the time series: $V_2 = -41.94$ (left, lower red curve), -26.00 (left, upper red curve), -40.23 (right, lower red curve), and -18.84 (right, upper red curve). Flow is counterclockwise. Note that for $C_1 = 0.8$ (left), the orbits adhere very closely to the nullclines in the silent and active phases, and the maximal V_1 drops significantly between the cycles shown. For $C_1 = 80$ (right), the orbits deviate from the nullclines much more, and the difference in maximal V_1 values, even between the first and last spikes of the burst, is significantly smaller.*

The mechanism for the gradual decay of V_1 spike amplitudes in the three-time-scale system was explained in section 3.2 (Figures 16 and 17) and depends on the fact that trajectories closely follow the V_2-dependent V_1-nullclines in the projection onto (V_1, w_1)-space in between fast jumps in V_1. Equivalently, in the projection onto (V_1, w_1, V_2)-space, V_2 has a strong effect on the shape of $\mathcal{M}_s$, which trajectories follow between these fast jumps. In the (3S, 1SS) scaling, however, $\mathcal{M}_s$ no longer plays a role and the oscillations in the projection to (V_1, w_1) pull away from the V_1-nullclines and lose their relaxation character. As a result, the V_1 amplitude becomes less varied across spikes (Figure 25). This effect persists across all g_{syn} values that yield V_1 spiking before V_2 jumps up in the (3S, 1SS) system.

Figure 26 shows the attracting solution for the (3S, 1SS) case projected onto (V_1, V_2, w_2)-space. On the lower right of this figure, the trajectory follows an attracting branch of $\mathcal{M}_{ss}$ with low V_1 and V_2. When the trajectory reaches the fold where this branch ends, slow oscillations of V_1 begin, but V_2 remains slaved to w_2, evolving on the superslow time scale, until a fold of the V_2-nullcline in the projection onto (V_2, w_2)-space is reached (although this projection is not shown, the fold is indicated by the green circle in Figure 26) and the slow

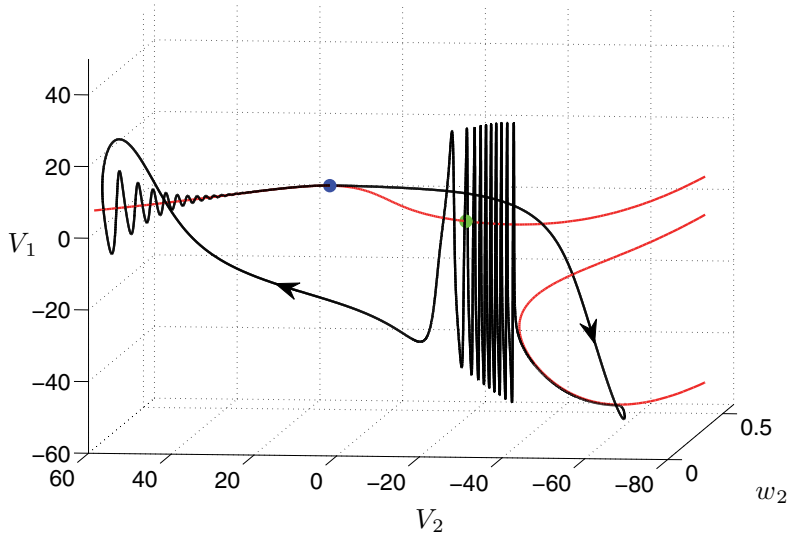

Figure 26. *Projection of the attracting solution (black curve) of the (3S, 1SS) system with* $g_{\text{syn}} = 4.1$, $C_1 = 80$, $\phi_2 = 0.0001$ *onto* (V_1, V_2, w_2)*-space. Red curves denote* $\mathcal{M}_{ss}$*, and blue and green circles mark two folds of* $\mathcal{M}_{ss}$.

transition to the next phase of the solution, with V_2 elevated, occurs. In the (3S, 1SS) regime, the branch of $\mathcal{M}_{ss}$ to the left of the blue circle is stable with respect to the three-dimensional slow system, and when the trajectory jumps up from the fold of the V_2-nullcline, it converges with damped oscillations in V_1 to this branch. This stability contrasts with the instability of $\mathcal{M}_{ss}$ for the (1F, 2S, 1SS) system with $g_{syn} = 4.1$ seen in Figure 14, which corresponds to the instability of the critical points of the v_2-frozen system (2.17) with elevated v_2 since V_2 is slaved to the superslow flow of w_2 during the relevant solution segment in the (1F, 2S, 1SS) case. Thus, the grouping of time scales can significantly alter the behavior of V_1 and w_1 in the regime where V_2 is elevated for $g_{syn} = 4.1$. After the damped V_1 oscillations, the trajectory jumps from a fold of $\mathcal{M}_{ss}$ (blue circle) back to the attracting branch of $\mathcal{M}_{ss}$ at low V_1 and V_2 (Figure 26) and another solution cycle begins.

Under rescaling to a (1F, 3S) system, a different type of trajectory is observed (Figure 24, bottom). The solution exhibits prolonged V_2 spikes as in the (1F, 3S) case with $g_{syn} = 1.0$ (Figure 23), but there are now multiple V_1 spikes per cycle because the trajectory can jump up from $\mathcal{M}_s^l$ with smaller V_2 than it could with $g_{syn} = 1.0$. The solution is quite different from that of the (1F, 2S, 1SS) system, lacking the rapid V_1 spikes and the transition from decrementing to constant amplitude spikes seen for (1F, 2S, 1SS) (Figure 25, top left).

In summary, neither of these two-time-scale systems captures the full features of the oscillating solution generated by (1.1) with $g_{syn} = 4.1$. The three-time-scale system has distinctive solutions with two groups of rapid V_1 spikes per cycle, one with decrementing amplitude and one with constant amplitude, but neither of the rescaled systems has solutions with both types of V_1 spikes. We therefore conclude that the solution shown in the second panel of Figure 2 represents an intrinsically three-time-scale phenomenon.

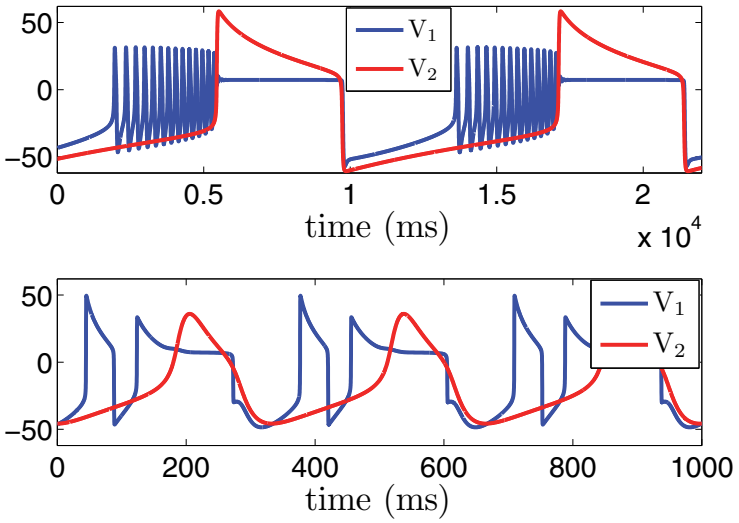

Figure 27. *Time series of* (1.1) *with* $g_{\rm syn} = 5.1$. *Top: (3S, 1SS) case corresponding to the choice* $C_1 = 80$, $\phi_2 = 0.0001$. *Bottom: (1F, 3S) case, with* $C_1 = 0.8$, $\phi_2 = 0.01$. *Other parameters as in Table 1.*

4.3. $g_{syn} = 5.1$: Direct transition to a depolarized plateau. When the time scale separation is exaggerated in the (1F, 2S, 1SS) system with $g_{syn} = 5.1$, the qualitative form of the solution, shown in Figure 2, does not change, nor does the relevance of the mechanisms shown in Figures 18–21. In particular, the V_1 time series includes a group of rapid spikes with decrementing amplitudes, followed by a depolarized plateau.

A time series obtained after rescaling to a (3S, 1SS) system with $g_{syn} = 5.1$ is shown in Figure 27 (top panel). As with $g_{syn} = 4.1$, this rescaling eliminates the gradual decrease of V_1 spike amplitudes, again due to the loss of relevance of $\mathcal{M}_s$ or, equivalently, the loss of relaxation oscillator character in the (V_1, w_1) oscillations; by similar arguments, varying g_{syn} away from 5.1 cannot restore this property. A second, subtle change is that the transition from large V_1 spikes to a V_1 plateau features a gradual damping in the two-time-scale case, evident during the abrupt increase in V_2, that is absent with three time scales. Recall that in the (1F, 2S, 1SS) case, this transition occurs while the orbit is following a solution segment of the two-dimensional slow layer problem. Linearization of this problem about the equilibrium point to which the solution segment converges, on $\mathcal{M}_{ss}$, yields a matrix with eigenvalues that can be shown to be real and negative for the (1F, 2S, 1SS) system; hence, the slow layer solution converges without damped oscillations to this equilibrium point. The situation is different in the (3S, 1SS) case. The solution segment during the V_2 jump is described by a solution of a three-dimensional slow layer problem. A calculation shows that the matrix obtained by linearizing this slow layer system about its equilibrium point on $\mathcal{M}_{ss}$ has eigenvalues of negative real part, but these can be complex. Thus, a possibility arises for subthreshold oscillations, and we observe these numerically for $g_{syn} = 5.1$ and other nearby values.

In the (1F, 3S) regime (Figure 27, bottom panel), the solution with $g_{syn} = 5.1$ is qualitatively similar to that obtained in the (1F, 3S) scaling with $g_{syn} = 4.1$, with similar mechanisms

involved. In particular, there is no convergence to an equilibrium point of a slow system (i.e., a point on $\mathcal{M}_{ss}$) during the active phase but instead an increase and decrease in all three slow variables, w_1, V_2, w_2. The V_1 time course is determined by the path of the slow system solution along $\mathcal{M}_s$, showing a gradual, nonmonotonic decay as V_2 increases that is quite distinct from the abrupt transition from spiking to plateau arising with three time scales.

In summary, the attracting solution of the (1F, 2S, 1SS) system with $g_{syn} = 5.1$ has two distinguishing features: a phase of rapid V_1 spikes of decrementing amplitudes and an abrupt transition to a depolarized plateau. The first of these is lost in both two-time-scale versions of the system that we considered. The second may in principle occur with a rescaling to (3S, 1SS), but is lost in the parameter regime we use; instead, subthreshold oscillations are seen during the transition. However, the effect is visually rather subtle and thus may not be relevant to efforts to model experimental data. Based on the spike amplitude modulation, at least, we can still conclude that the solution shown in Figure 2 with $g_{syn} = 5.1$ is an intrinsically three-time-scale phenomenon, but we acknowledge that the distinctiveness of the three-time-scale case is more limited than with the other g_{syn} values we discussed.

5. Discussion.

In this work, we have considered the dynamics of a model system with three time scales. Our analysis has been done from two perspectives, both based on the ideas of fast-slow decomposition: the first involves concatenation of segments of solutions of various subsystems (reduced and layer problems), while the second considers the interaction of two potentially oscillating systems (one fast-slow and the other slow-superslow). Both perspectives are commonly used in the context of two-time-scale dynamical systems, and our work illustrates that they can be extended to the three-time-scale setting and that they complement each other well. In particular, the concatenation method provides a clear view of how characteristics of trajectories relate to the features of slow and superslow manifolds and their folds, while the coupled oscillator approach helps elucidate how these manifold features arise. For $g_{syn} = 4.1$, for example, consideration of slow and superslow manifolds shows that an attracting branch of the superslow manifold intersects a fold of the critical manifold, yielding a direct transition from superslow to fast dynamics, while consideration of how nullclines of one oscillator respond to changes in another oscillator gives insight into the evolution of solution features (e.g., spike amplitudes) over time. We hope that these insights will guide other researchers undertaking similar analyses related to their problems of interest.

In addition to providing a helpful comparison of approaches, our analysis yields several insights. First, the fast-slow decomposition methods developed for two-time-scale systems do extend naturally to three-time-scale settings, and it is clear that this extension would carry over similarly to systems with more than three time scales as well. Second, there are natural mechanisms for transitions directly from superslow to fast dynamics, yet we generically do not expect transitions directly from fast to superslow, as these would require fast layer problem solutions to asymptote to limits that happen to be equilibria of certain slow systems as well. Besides superslow to fast transitions, we also observe transitions from superslow dynamics to fast-slow relaxation oscillations in some variables with continued superslow drift in others. This finding highlights a need for an averaging result for the three-time-scale setting, like the one that justifies use of a slow averaged system in a two-time-scale context when solutions combine fast oscillations and slow drift. Third, there is a limitation to the utility of frozen

systems for the analysis of coupled oscillator systems; full system dynamics can have features not predicted from bifurcation analysis based on frozen systems, as we see with $g_{syn} = 1.0$.

While parts of this work investigate rather specific details of solution features, we have followed our descriptive analysis with an investigation of which solution features are truly three-time-scale phenomena. Identifying solution features that require three time scales provides useful information for modeling studies, where a determination needs to be made about how many time scales to include in a model to represent some given experimental data. In fact, many of the solution features that we observe are lost under grouping to two time scales and hence can be said to require three time scales, at least in the system we have studied. This finding suggests that classifying disparate time scales into two groups should no longer be a default approach in modeling work. We also note that choices about how to group time scales determine the dimensionality of various subsystems that come into play, and the dimension of a subsystem constrains the types of solutions it can support; certain solution features will therefore only be observed in certain time scale groupings. In an arbitrary multiple time scale system, the number of time scales exhibited by a particular solution need not be as large as the number of distinct time scales in the system as a whole. An example occurs in system (1.1) for small g_{syn}; in this case, v_1 stays relatively steady and does not spike, so the fast time scale is not observed in the attracting solution for the system. Hence, three-time-scale effects can be destroyed in our system by decreasing g_{syn}. However, since the (v_2, w_2) system decouples, there will always be slow and superslow components to solutions and, once g_{syn} is large enough that v_1 becomes active, three time scales will be manifest in solutions. Thus, while it is generally the case that three-time-scale effects can be removed by varying a system parameter rather than by changing the time scale separation as we have done in this article, this possibility is not of interest in our system.

Ours is not the first work to provide mathematical analysis of a three-time-scale system. Several papers in this area have focused on mixed-mode oscillations (MMOs) supported by three time scales. The initial approach was to consider a three-dimensional system where the right-hand sides were $\mathcal{O}(1), \mathcal{O}(\epsilon), \mathcal{O}(\epsilon^2)$, respectively [17]; MMOs were shown to emerge through an effect analogous to a slow drift through a canard explosion. Certain higher dimensional systems were also shown to reduce to similar three-dimensional systems with the same structure [22, 13]; see also [4].

The paper closest to ours is [18], which also considers two coupled systems, one fast-slow and one slow-superslow, with unidirectional coupling such that the slow-superslow oscillator forces the fast-slow system. Some similar features are seen in solutions to our model and those from [18], including periods of rapid oscillation of relaxation type (called the pulsatile phase in [18]) and segments where all variables are changing on the superslow time scale (occurring within the surge phase in [18]). However, in [18], the slow variable from the slow-superslow oscillator appears in the slow equation of the fast-slow oscillator, rather than in the fast equation as in our model. An important consequence is that while our model can exhibit amplitude modulation during the fast spiking phase (as in, for instance, the upper right and lower panels of Figure 2) because the position and shape of the nullcline for the fast variable is modified by the coupling term, this effect is absent in the model of [18] where the coupling moves the relative positions of the nullclines but does not alter their shape. The focus in [18] is also somewhat different to ours; they are interested in determining the dynamical mechanisms

for the MMOs found in their system, whereas we have concentrated on identifying features of the dynamics that are truly three-time-scale phenomena. We note that MMOs are likely to occur in our system in certain parameter regimes, but we have not looked for them.

Ha and Kuznetsov [9] also considered a three-time-scale model, describing the interactions of voltage and calcium concentration in a neuronal soma linked with a neuronal dendrite. Their work focused on mechanisms leading to two different types of oscillations, one involving the fast and intermediate time scales and another based on fast and slow components, rather than solution features emerging from the concurrent interaction of all three time scales. A recent paper by Vo, Bertram, and Wechselberger [31] considered solutions of a four-dimensional, three-time-scale model of electrical activity and calcium signaling in a pituitary lactotroph, focusing on solutions such as MMOs that can appear in systems with two time scales. The authors considered the effect of grouping the time scales into two groups in two different ways and showed that the dynamics of these rescaled models could be understood as different unfoldings of the full three-time-scale system. The two two-time-scale approaches were compared, were shown to provide different insights, and were unified via a fully three-time-scale representation, but little consideration was given to identifying dynamic features that are specifically three-time-scale phenomena, as we do. Franci, Drion, and Sepulchre [8] considered bursting in conductance-based models of neurons and proposed a three-time-scale "normal form" for the phenomenon. The focus was on explaining how observed bursting behavior might arise in unfoldings of the normal form, rather than on identifying phenomena that are intrinsically three-time-scale. Indeed, many earlier analyses of bursting behavior have shown that only two time scales are needed in order to observe bursting solutions, and the work of [8] shows how previously observed two-time-scale bursters might be transformed into one another by superslow variation of system parameters. Other models with three time scales have been discussed in the recent literature (see, e.g., [10, 11, 19]) but, again, the analysis presented arises mostly from grouping the time scales into two groups and there is little insight into intrinsically three-time-scale phenomena.

In the emerging study of systems with more than two time scales, there are many directions for future work, even without considering complications such as stochasticity, forcing, or delays. As in other earlier work (e.g., [18]), we have considered a specific form of coupling such that our model system can be thought of as one oscillator forcing another. Preliminary investigations suggest that in the scenarios we have considered, the inclusion of bidirectional coupling has surprisingly little influence on solution features. Nonetheless, there are many variations on the coupling among time scales that arise in other model systems and should be considered in future work. The consideration of bidirectional coupling is likely to be particularly important for understanding the dynamics of our main motivating example, the oscillatory dynamics of neurons, where membrane potential and cytoplasmic Ca^{2+} concentration can each influence the evolution of the other. Note also that our ML models were tuned individually to be Type I oscillators, with an onset of oscillations through a SNIC bifurcation under variation of the applied current parameter I_i, yet the coupling nonetheless induced oscillations in (V_1, w_1) via an AH bifurcation with respect to changes in V_2. This effect would not change with intrinsically Type II oscillators, so we expect little difference there relative to what we have considered, but this expectation still remains to be confirmed.

From a more theoretical point of view, there is much work to be done to explore folded

singularities that can arise and affect solutions in systems with three or more time scales. In the solutions that we considered, trajectories pass close to folded singularities, yet these have little influence on the resulting dynamics. This is unlikely to always be the case, however (see also [31]), and a comprehensive theory of folded singularities in systems with more than two time scales is needed. There are also many other forms of dynamics that one could consider that are outside the coupled oscillator framework altogether, and these will likely yield a variety of three-time-scale phenomena beyond those that we have identified.

6. Appendix. Here we present details of the nondimensionalization of (1.1). From numerical simulations of this system, we find that the membrane potential for the uncoupled ML oscillators typically lies between $-70\,\mathrm{mV}$ and $60\,\mathrm{mV}$. Correspondingly, we define $T_w = \max(1/\tau_w(V_i))$ over the range $V_i \in [-70, 60]$ and then define $t_w(V_i)$, a rescaled version of $\tau_w(V_i)$, by $t_w(V_i) = T_w \tau_w(V_i)$. We also define $g_{\max}$ to be the maximum of the three conductances g_{Ca}, g_{K}, and g_{L}. Substituting these expressions into (1.1a)–(1.1d) and rearranging, we obtain the following dimensionless system:

$$\frac{C_1}{Q_t \cdot g_{\max}} \frac{dv_1}{d\tau} = \bar{I}_1 - \bar{g}_{\mathrm{Ca}} m_\infty(v_1)(v_1 - \bar{V}_{\mathrm{Ca}}) - \bar{g}_{\mathrm{K}} w_1 (v_1 - \bar{V}_{\mathrm{K}}) - \bar{g}_{\mathrm{L}}(v_1 - \bar{V}_{\mathrm{L}}) - \bar{g}_{\mathrm{syn}} S(v_2)(v_1 - \bar{V}_{\mathrm{syn}}), \tag{6.1a}$$

$$\frac{1}{\phi_1 Q_t T_{w_1}} \frac{dw_1}{d\tau} = \frac{1}{t_w(v_1)}(w_\infty(v_1) - w_1), \tag{6.1b}$$

$$\frac{C_2}{Q_t \cdot g_{\max}} \frac{dv_2}{d\tau} = \bar{I}_2 - \bar{g}_{\mathrm{Ca}} m_\infty(v_2)(v_2 - \bar{V}_{\mathrm{Ca}}) - \bar{g}_{\mathrm{K}} w_2 (v_2 - \bar{V}_{\mathrm{K}}) - \bar{g}_{\mathrm{L}}(v_2 - \bar{V}_{\mathrm{L}}), \tag{6.1c}$$

$$\frac{1}{\phi_2 Q_t T_{w_2}} \frac{dw_2}{d\tau} = \frac{1}{t_w(v_2)}(w_\infty(v_2) - w_2)\,, \tag{6.1d}$$

with dimensionless parameters $\bar{I}_x = I_x/(Q_v \cdot g_{\max})$, $\bar{g}_x = g_x/g_{\max}$, and $\bar{V}_x = V_x/Q_v$.

Since we expect $V_i \in [-70, 60]$, a suitable choice for the voltage scale is $Q_V = 100\,\mathrm{mV}$. We also see that values of $m_\infty(V_i)$, $w_\infty(V_i)$, and w_i all lie in the range $[0, 1]$. For the choice of parameters specified in Table 1, the maximum conductance is g_{K}, so we have $g_{\max} = g_{\mathrm{K}}$. Numerical evaluation of $1/\tau_w(V_i)$ for $V_i \in [-70, 60]$ shows that $T_w \approx 5.3\,\mathrm{ms}^{-1} = O(10)\,\mathrm{ms}^{-1}$. Using these values we see that all terms on the right-hand sides of (6.1a)–(6.1d) are bounded (in absolute value) by one.

The coefficients of the derivatives on the left-hand sides of (6.1a)–(6.1d) now reveal the relative rates of evolution of the variables. We find that $C_1/g_{\max} = O(1)\,\mathrm{ms}^{-1}$, $1/(\phi_1 T_w) \approx C_2/g_{\max} = O(10)\,\mathrm{ms}^{-1}$, and $1/(\phi_2 T_w) = O(100)\,\mathrm{ms}^{-1}$, from which we conclude that v_1 evolves on a fast time scale, w_1 and v_2 evolve on a slow time scale, and w_2 evolves on a superslow time scale. We choose the slow time scale as our reference time, i.e., pick $Q_t = 10\,\mathrm{ms}$, and set

$$\varepsilon_1 := \frac{C_1}{Q_t \cdot g_{\max}} \ll 1\,, \qquad \varepsilon_2 := \phi_2 Q_t T_w \ll 1\,, \tag{6.2a}$$

$$R_{w_1} := \phi_1 Q_t T_w\,, \qquad R_{v_2} := \frac{Q_t \cdot g_{\max}}{C_2}\,. \tag{6.2b}$$

As a result, the dimensionless system (6.1) becomes the system (2.2) given in section 2, namely,

$$\varepsilon_1 \frac{dv_1}{d\tau} = \bar{I}_1 - \bar{g}_{\mathrm{Ca}} m_\infty(v_1)(v_1 - \bar{V}_{\mathrm{Ca}}) - \bar{g}_{\mathrm{K}} w_1 (v_1 - \bar{V}_{\mathrm{K}}) - \bar{g}_{\mathrm{L}}(v_1 - \bar{V}_{\mathrm{L}}) - \bar{g}_{\mathrm{syn}} S(v_2)(v_1 - \bar{V}_{\mathrm{syn}}) := f_1(v_1, v_2, w_1), \tag{6.3a}$$

$$\frac{dw_1}{d\tau} = R_{w_1} \frac{1}{t_w(v_1)} (w_\infty(v_1) - w_1) := g_1(v_1, w_1), \tag{6.3b}$$

$$\frac{dv_2}{d\tau} = R_{v_2}(\bar{I}_2 - \bar{g}_{\mathrm{Ca}} m_\infty(v_2)(v_2 - \bar{V}_{\mathrm{Ca}}) - \bar{g}_{\mathrm{K}} w_2 (v_2 - \bar{V}_{\mathrm{K}}) - \bar{g}_{\mathrm{L}}(v_2 - \bar{V}_{\mathrm{L}})) := f_2(v_2, w_2), \tag{6.3c}$$

$$\frac{dw_2}{d\tau} = \varepsilon_2 \frac{1}{t_w(v_2)} (w_\infty(v_2) - w_2) := \varepsilon_2 g_2(v_2, w_2)\,, \tag{6.3d}$$

with small parameters ε_1 and ε_2, where R_{w_1} and R_{v_2} are dimensionless parameters bounded by one.

Acknowledgment. J. Rubin thanks B. Krauskopf and H. Osinga at the University of Auckland.

REFERENCES

[1] A. Bose, Y. Manor, and F. Nadim, *Bistable oscillations arising from synaptic depression*, SIAM J. Appl. Math., 62 (2001), pp. 706–727.

[2] F. Clément and J.-P. Françoise, *Mathematical modeling of the GnRH pulse and surge generator*, SIAM J. Appl. Dyn. Syst., 6 (2007), pp. 441–456.

[3] S. Daun, J. E. Rubin, and I. A. Rybak, *Control of oscillation periods and phase durations in half-center central pattern generators: A comparative mechanistic analysis*, J. Comput. Neurosci., 27 (2009), pp. 3–36.

[4] P. De Maesschalck, E. Kutafina, and N. Popović, *Three time-scales in an extended Bonhoeffer-Van der Pol oscillator*, J. Dynam. Differential Equations, 26 (2014), pp. 955–987.

[5] M. Desroches, J. Guckenheimer, B. Krauskopf, C. Kuehn, H. M. Osinga, and M. Wechselberger, *Mixed-mode oscillations with multiple time scales*, SIAM Rev., 54 (2012), pp. 211–288.

[6] B. Ermentrout and D. Terman, *Mathematical Foundations of Neuroscience*, Springer, 2010.

[7] N. Fenichel, *Persistence and smoothness of invariant manifolds for flows*, Indiana Univ. Math. J., 21 (1971), pp. 193–225.

[8] A. Franci, G. Drion, and R. Sepulchre, *Modeling the modulation of neuronal bursting: A singularity theory approach*, SIAM J. Appl. Dyn. Syst., 13 (2014), pp. 798–829.

[9] J. Ha and A. Kuznetsov, *Frequency switching in a two-compartmental model of the dopaminergic neuron*, J. Comput. Neurosci., 30 (2011), pp. 241–254.

[10] E. Harvey, V. Kirk, H. M. Osinga, J. Sneyd, and M. Wechselberger, *Understanding anomalous delays in a model of intracellular calcium dynamics*, Chaos, 20 (2010), 045104.

[11] E. Harvey, V. Kirk, J. Sneyd, and M. Wechselberger, *Multiple timescales, mixed mode oscillations and canards in models of intracellular calcium dynamics*, J. Nonlinear Sci., 21 (2011), pp. 639–683.

[12] E. M. Izhikevich, *Dynamical Systems in Neuroscience: The Geometry of Excitability and Bursting*, MIT Press, Cambridge, MA, 2006.

[13] J. Jalics, M. Krupa, and H. G. Rotstein, *Mixed-mode oscillations in a three time-scale system of odes motivated by a neuronal model*, Dyn. Syst., 25 (2010), pp. 445–482.

[14] C. K. R. T. Jones, *Geometric singular perturbation theory*, in Dynamical Systems (Montecartini Terme, 1994), Springer-Verlag, Berlin, New York, 1995, pp. 44–118.

[15] T. J. Kaper, *An introduction to geometric methods and dynamical systems theory for singular perturbation problems*, in Analyzing Multiscale Phenomena Using Singular Perturbation Methods, Proc. Sympos. Appl. Math. 56, AMS, Providence, RI, 1999, pp. 85–131.
[16] J. Keener and J. Sneyd, *Mathematical Physiology*, Springer, 2008.
[17] M. Krupa, N. Popović, and N. Kopell, *Mixed-mode oscillations in three time-scale systems: A prototypical example*, SIAM J. Appl. Dyn. Syst., 7 (2008), pp. 361–420.
[18] M. Krupa, A. Vidal, M. Desroches, and F. Clément, *Mixed-mode oscillations in a multiple time scale phantom bursting system*, SIAM J. Appl. Dyn. Syst., 11 (2012), pp. 1458–1498.
[19] K. Lee, W. Duan, J. Sneyd, and A. E. Herbison, *Two slow calcium-activated afterhyperpolarization currents control burst firing dynamics in gonadotropin-releasing hormone neurons*, J. Neurosci., 30 (2010), pp. 6214–6224.
[20] C. Morris and H. Lecar, *Voltage oscillations in the barnacle giant muscle fiber*, Biophys. J., 35 (1981), pp. 193–213.
[21] C. Park and J. E. Rubin, *Cooperation of intrinsic bursting and calcium oscillations underlying activity patterns of model pre-Bötzinger complex neurons*, J. Comput. Neurosci., 34 (2013), pp. 345–366.
[22] N. Popović, *Mixed-mode dynamics and the canard phenomenon: Towards a classification*, J. Phys. Conf. Ser., 138 (2008), 012020.
[23] J. Rinzel and G. B. Ermentrout, *Analysis of neural excitability and oscillations*, in Methods in Neuronal Modeling: From Synapses to Networks, 2nd ed., C. Koch and I. Segev, eds., MIT Press, Cambridge, MA, 1998, pp. 251–291.
[24] J. Rubin, *Bursting induced by excitatory synaptic coupling in non-identical conditional relaxation oscillators or square-wave bursters*, Phys. Rev. E, 74 (2006), 021917.
[25] J. Rubin and D. Terman, *Geometric singular perturbation analysis of neuronal dynamics*, in Handbook of Dynamical Systems, Vol. 2: Towards Applications, B. Fiedler, ed., Elsevier, 2002.
[26] D. Somers and N. Kopell, *Rapid synchronization through fast threshold modulation*, Biol. Cybern., 68 (1993), pp. 393–407.
[27] D. Terman, N. Kopell, and A. Bose, *Dynamics of two mutually coupled inhibitory neurons*, Phys. D, 117 (1998), pp. 241–275.
[28] D. Terman and D. Wang, *Global competition and local cooperations in a network of neural oscillators*, Phys. D, 81 (1995), pp. 148–176.
[29] K. Tsumoto, H. Kitajima, T. Yoshinaga, K. Aihara, and H. Kawakami, *Bifucations in Morris-Lecar model*, Neurocomputing, 69 (2006), pp. 293–316.
[30] A. Vidal and F. Clément, *A dynamical model for the control of the gonadotrophin-releasing hormone neurosecretory system*, J. Neuroendocrinology, 22 (2010), pp. 1251–1266.
[31] T. Vo, R. Bertram, and M. Wechselberger, *Multiple geometric viewpoints of mixed mode dynamics associated with pseudo-plateau bursting*, SIAM J. Appl. Dyn. Syst., 12 (2013), pp. 789–830.
[32] M. Wechselberger, *A propos de canards (apropos canards)*, Trans. Amer. Math. Soc., 364 (2012), pp. 3289–3309.